Chapter 4

The split semi-Lagrangian solution procedure

4.1 Introduction

In Chapter 3 the pressure coordinate equation set of White (1989) is transformed to σ coordinates, and the properties of the equation set are discussed. The equation set (3.64) to (3.68) (or (3.82) to (3.85) in two spatial dimensions) will from now on be refered to as the "quasi-elastic σ coordinate equations", or just as the "quasi-elastic equations". In this Chapter, an adiabatic kernel for a new mesoscale numerical model based on these equations is described. The main and novel feature of the new dynamic kernel, is that it uses a split semi-Lagrangian procedure to solve the quasi-elastic equations on a nonstaggered grid. The numerical formulation is able to deal with nonzero topography. In fact, the dynamic kernel is developed with the aim to closely parallel the formalism of existing operational hydrostatic σ coordinate models. In this way, the convenient conversion of existing hydrostatic σ coordinate models to non-hydrostatic models based on the quasi-elastic equations is facilitated.

Numerical solutions of the σ coordinate MP and NHAD models all utilised explicit leapfrog solution procedures (e.g. Xue and Thorpe, 1991; Miranda and James, 1992; Room et al., 2001). In these numerical solutions, the maximum size of time step allowed is limited by the well-known CFL condition. The absence of sound waves propagating in the vertical greatly alleviates the restriction on the time step in the MP model, especially when high vertical resolution is required (Xue and Thorpe, 1991). However, in the σ coordinate applications of the MP model, the presence of Lamb waves still places a significant restriction on the maximum size of time-step allowed (Room et al., 2001). In the NHAD model the additional filtering of Lamb waves results in additional alleviation of the restriction placed on the maximum size of time step by the CFL condition (Room et al., 2001). However, the maximum size of time step used remains

restricted to some extent by the by the presence of fast travelling gravity waves. Also, the σ coordinate employed in the NHAD model in order to achieve the filtering of Lamb waves (see Chapter 2; Room et al., 2001), is likely to restrict the application of the model to relatively small domains and short spatial scales (see Chapter 2).

The solution procedure presented in this Chapter employs a split semi-Lagrangian approach to solve the quasi-elastic σ coordinate equations. That is, for numerical solution the equations are split into an advective and non-advective part. The slow advection process is treated during a semi-Lagrangian advection step that may employ a large time step. Indeed, it is shown that the split semi-Lagrangian scheme can be used to obtain stable integrations at large Courant numbers present during the advection step. Hereafter the remaining terms, which describe fast moving waves, are treated explicitly during an adjustment phase that employs a smaller time step. It may be noted that the numerical modelling of cloud microphysics and condensation can potentially be incorporated in another adjustment phase, that may also require a small time step for the adequate modelling of cloud thermodynamics and precipitation formation. The numerical procedure presented does not require linearization of any kind. It may be noted that although a number of split semi-Lagrangian models solving the hydrostatic equations have been developed (Bates and McDonald, 1982; Bates, 1984; McGregor, 1986; Leslie and Purser, 1991), there have been only a few applications of split semi-Lagrangian procedures in the context of nonhydrostatic equation sets.

An important feature of the new numerical scheme is that it is formulated on a nonstaggered grid, also referred to as an A-grid (e.g. Mesinger and Arakawa, 1976; Arakawa and Lamb, 1977). A nonstaggered grid is appealing to use in semi-Lagrange discretizations, since one set of trajectories can be used to provide common departure points for all variables (McGregor, 2005). On a staggered grid, at least one more set of trajectories is needed to calculate the departure points of variables at staggered positions. Also, the wind components need to be obtained by averaging procedures at the staggered grid points where they are not calculated explicitly, in order to facilitate the calculation of departure points associated with these staggered grid points. This may possibly impact negatively on numerical consistency and accuracy. Once the different sets of trajectories have been calculated on the staggered grid, different sets of grid point interpolations are needed to calculate the values of variables at the different sets of departure points. Only a single set of interpolations is required on the nonstaggered grid for the single set of departure points (Leslie and Purser, 1991). Thus, from the viewpoint of numerical accuracy and computational economy, there exist strong motivation for the use of nonstaggered grids in semi-Lagrange discretizations of the atmospheric equations. However, there are only a few atmospheric models that employ a nonstaggered grid (e.g. Kaplan et al., 1982; Kalnay-Rivas and Hoitsma, 1979; Purser and Leslie, 1988; Leslie and Purser,

1991). The main reason for the unpopularity of the A-grid, is that the spatial discretization of the shallow water equations reveals that the nonstaggered grid has poor dispersion properties compared to the usual staggered grids (e.g. Winninghoff 1968; Mesinger and Arakawa, 1976; Arakawa and Lamb, 1977; Schoenstadt, 1978).

Conversely, the staggered C-grid has become very popular for use in atmospheric models, because it has good dispersion behaviour for large Rossby radius of deformation (defined relative to the grid spacing) (McGregor, 2005). However, as discussed in the previous paragraph, the C-grid and other staggered grids are somewhat problematic to use for semi-Lagrangian solution procedures. Recently, a reversible staggering arrangement of variables has been proposed to obtain improved gravity wave dispersion characteristics while still using a formulation of the primitive equations on the A-grid (McGregor, 1995). The basic idea is to perform a transformation from the A-grid to a C-grid for the calculation of the gravity wave terms, using a new reversible interpolation scheme based on the generalized Vandermonde method. The so called R-grid scheme ensures consistent transformation of variables between staggered and nonstaggered positions, and has excellent dispersion characteristics for the geostrophic adjustment of the shallow-water equations (McGregor, 2005). The reversible staggering approach is most accurately performed in a cyclic domain (McGregor, 2005). For the limited-area, meso-scale applications of the model developed in this study, the reversible staggering approach is certainly an option in order to improve on the poor gravity wave dispersion properties of the nonstaggered grid. However, the method will need modification for the non-cyclic boundary conditions commonly encountered in in limited-area modelling. Instead, an alternative approach has been selected in this study, and that is to improve the gravity wave dispersion properties of the A-grid by means of high-order spatial differencing and filtering. It should also be noted that the focus in this study is on the development of a new meso-scale model. Although the accurate treatment of gravity waves is of fundamental importance for such a model, the geostrophic adjustment process does not play an important role at the spatial and time scales that the model will be applied to (see Chapter 5).

Thus, the distinguishing feature of the new numerical scheme developed is the split semi-Lagrangian approach that is used on a nonstaggered grid. This approach ensures numerical accuracy and computational economy during the calculation of departure points, and the corresponding interpolations. High-order spatial filtering is used to filter the smallest resolvable gravity waves on the nonstaggered grid, whilst the waves that are resolved may be treated accurately by employing high order spatial differencing. The three main building blocks used to construct the split semi-Lagrangian scheme are discussed in the next three sections. Firstly the semi-Lagrangian scheme applied in the model to numerically represent the advection process, is discussed in section 4.2. In particular, the method developed by McGregor (1993) to evaluate the departure

points of fluid parcels is presented. The phase and amplitude accuracy properties resulting from the bicubic interpolation scheme that is used to evaluate the values of variables at departure points (McDonald, 1984) are also analysed. Secondly, high-order spatial differencing formulas for use on the nonstaggered grid are presented in section 4.3, following Purser and Leslie (1988). Thirdly, the high-order spatial filtering used to filter the shortest resolvable gravity waves from the nonstaggered grid (Shapiro, 1975), are discussed in section 4.4. The split semi-Lagrangian solution procedure is outlined in section 4.5. The procedure involves the solution of an elliptic equation for the geopotential at each adjustment time-step; the iterative technique used is discussed in section 4.6. In section 4.7 the frequency response of the forward-backward scheme used in the adjustment step is analysed. The gravity wave response to discretization on the nonstaggered grid is evaluated in section 4.8. The effect of high-order spatial differencing on improving the frequency (or phase speed) accuracy of the discretized waves is discussed in particular. Lateral and vertical boundary conditions for the model are formulated in section 4.9. In section 4.10, the properties of the newly developed scheme are compared to those of the numerical schemes used in the MP and NHAD models. A discussion of the results obtained and some conclusions can be found in section 4.11.

4.2 The semi-Lagrangian advection scheme

During the last 20 years, semi-Lagrangian schemes for treating horizontal and (or) vertical advection in NWP and climate simulation models have become increasingly popular (e.g. Robert, 1981, 1982; Bates and McDonald, 1982; McDonald, 1986; McGregor, 1987; Ritchie, 1987; Tanguay et al., 1989; McGregor, 1993; Bates et al., 1995; Davies et al., 2005). This popularity stems from the large advection time-steps permitted by semi-Lagrangian advection schemes compared to Eulerian schemes, without compromising numerical stability. The semi-Lagrangian approach for solving the advection terms consists of two steps: The calculation of the departure point of each grid point in the model, and secondly, the evaluation of variables at the departure point by means of spatial interpolation. In this study, an efficient procedure developed by McGregor (1993) is applied to calculate the departure points, whilst bicubic spatial interpolation (McDonald, 1984) is used to evaluate the values of variables at the departure points. These two procedures are discussed in the following two sections.

4.2.1 McGregor's method for the calulation of the departure points

An Eulerian procedure that avoids both interpolation and iteration for determining the departure points of trajectories was proposed by McGregor (1993). The technique can achieve a high degree of accuracy, is somewhat simpler and more economical than other schemes, and can be applied to semi-Lagrangian models on the plane or on the sphere. The procedure has been applied sucess-

fully to the simulation of horizontal advection in the hydrostatic semi-implicit semi-Lagrangian regional models DARLAM and the variable resolution global model C-CAM (McGregor, 1993, 1996; McGregor and Dix, 2001; McGregor et al., 2002). In this section, the method of McGregor (1993) is formulated for application in the split semi-Lagrangian procedure used to solve the nonhydrostatic quasi-elastic equations (see section 4.5). The procedure is used to treat both horizontal and vertical advection in the new model.

Following the discussion by McGregor (1993), let $\mathbf{r}(t)$ denote a member of a set of vectors moving with the fluid. With each grid point, a different vector $\mathbf{r}(t)$ will be associated at time t. Thus, the grid points are the prescribed arrival locations of the vectors move with the fluid. To advance the model integration from time τ to $\tau + \Delta t$, a vector $\mathbf{r}(\tau + \Delta t)$ is set up at the position of each arrival grid point. It is required to find the starting position of the vector at the preceding time step, namely $\mathbf{r}(\tau)$. This may be expressed in terms of the Taylor series

$$\mathbf{r}(\tau) = \mathbf{r}(\tau + \Delta t) + \Sigma_{n=1}^{\infty} \frac{(-\Delta t)^n}{n!} \frac{d^n \mathbf{r}}{dt^n}(\tau + \Delta t), \tag{4.1}$$

where

$$\frac{d^n \mathbf{r}(t)}{dt^n} = \frac{d}{dt}\left[\frac{d^{n-1}\mathbf{r}(t)}{dt^{n-1}}\right] \quad n = 2, 3, ... \tag{4.2}$$

and the total derivative has the usual definition of a time derivative following the motion of a parcel,

$$\frac{d}{dt} = \frac{\partial}{\partial t} + \mathbf{u} \cdot \bar{\nabla}. \tag{4.3}$$

Here $\mathbf{u} = d\mathbf{r}/dt$ is the velocity of the fluid at position $\mathbf{r}(t)$ and $\bar{\nabla}$ is the spatial gradient operator. In (4.3) the time derivative on the left-hand side is naturally viewed in a Lagrangian sense. The right-hand side allows its instantaneous evaluation at the same point in time and space via Eulerian derivatives (McGregor, 1993). However, if the Eulerian velocities change with time, it may be very cumbersome to evaluate the partial time derivatives for the higher order terms in (4.1) (McGregor, 1993). The scheme proposed by McGregor (1993) replaces the total time derivative (4.3) for use in (4.1) and (4.2) by the approximate formula

$$\frac{d}{dt} \approx \hat{\mathbf{u}} \cdot \bar{\nabla}. \tag{4.4}$$

Here $\hat{\mathbf{u}}$ represents the (Eulerian) velocity at the point in space corresponding to $\mathbf{r}(\tau + \Delta t)$, but evaluated at the intermediate time $\tau + \Delta t/2$. The above scheme using (4.1), (4.2) and (4.4), and retaining terms up to the Nth total time derivative is called a D_N scheme (McGregor, 1993). The velocity $\hat{\mathbf{u}}$ may be conveniently determinded by means of extrapolation in time from the known

velocities at previous time steps; a formula with third-order accuracy in time is given by Temperton and Staniforth (1987):

$$\mathbf{u} = \frac{1}{8}\left[15\mathbf{u}\left(\tau\right) - 10\mathbf{u}\left(\tau - \Delta t\right) + 3\mathbf{u}\left(\tau - 2\Delta t\right)\right] + O\left(\Delta t^3\right). \tag{4.5}$$

The idea behind the approximation (4.4) is that for advection purposes the velocities are considered to remain constant in an Eulerian sense over the time interval $(\tau, \tau + \Delta t)$ at their centered in time value (McGregor, 1993). A slight disavantage of the application of formula (4.5), is the need to store values of the wind field at three time-levels, although the scheme is formulated here for two time-level applications. The number of terms that should be retained in practice in the Taylor series (4.1) depends on the smoothness of the velocity field (McGregor, 1993). McGregor (1993) found only slight benefit in going beyond the D_3 scheme. The D_3 scheme has been implemented and used successfully in the hydrostatic regional model DARLAM (McGregor, 1993) and is also used in the more recently developed hydrostatic variable resolution global model C-CAM (McGregor, 1996; McGregor and Dix, 2001; McGregor et al., 2002). In Chapter 5, the D_N schemes for choices of N up to 3 are tested for cases of highly nonhydrostatic flow, and a recommendation of the most appropriate choice of N is made.

The calculation formulas for the three-dimensional departure points as determined by the D_1, D_2 and D_3 schemes are respectively:

$\mathbf{D_1}$ scheme:

$$\begin{bmatrix} x^* \\ y^* \\ \sigma^* \end{bmatrix} = \begin{bmatrix} x \\ y \\ \sigma \end{bmatrix} - \Delta t \begin{bmatrix} \hat{u} \\ \hat{v} \\ \hat{\dot{\sigma}} \end{bmatrix} \tag{4.6}$$

$\mathbf{D_2}$ scheme:

$$\begin{bmatrix} x^* \\ y^* \\ \sigma^* \end{bmatrix} = \begin{bmatrix} x \\ y \\ \sigma \end{bmatrix} - \Delta t \begin{bmatrix} \hat{u} \\ \hat{v} \\ \hat{\dot{\sigma}} \end{bmatrix} + \frac{\Delta t^2}{2!} \begin{bmatrix} \hat{u}\frac{\partial \hat{u}}{\partial x} + \hat{v}\frac{\partial \hat{u}}{\partial y} + \hat{\dot{\sigma}}\frac{\partial \hat{u}}{\partial \sigma} \\ \hat{u}\frac{\partial \hat{v}}{\partial x} + \hat{v}\frac{\partial \hat{v}}{\partial y} + \hat{\dot{\sigma}}\frac{\partial \hat{v}}{\partial \sigma} \\ \hat{u}\frac{\partial \hat{\dot{\sigma}}}{\partial x} + \hat{v}\frac{\partial \hat{\dot{\sigma}}}{\partial y} + \hat{\dot{\sigma}}\frac{\partial \hat{\dot{\sigma}}}{\partial \sigma} \end{bmatrix}$$

or, by introducing notation for the estimated acceleration along the trajectory,

$$\begin{bmatrix} x^* \\ y^* \\ \sigma^* \end{bmatrix} = \begin{bmatrix} x \\ y \\ \sigma \end{bmatrix} - \Delta t \begin{bmatrix} \hat{u} \\ \hat{v} \\ \hat{\dot{\sigma}} \end{bmatrix} + \frac{\Delta t^2}{2!} \begin{bmatrix} \hat{a}_{\hat{u}} \\ \hat{a}_{\hat{v}} \\ \hat{a}_{\hat{\dot{\sigma}}} \end{bmatrix} \tag{4.7}$$

D_3 scheme:

$$\begin{bmatrix} x^* \\ y^* \\ \sigma^* \end{bmatrix} = \begin{bmatrix} x \\ y \\ \sigma \end{bmatrix} - \Delta t \begin{bmatrix} \hat{u} \\ \hat{v} \\ \hat{\dot{\sigma}} \end{bmatrix} + \frac{\Delta t^2}{2!} \begin{bmatrix} \hat{a}_{\hat{u}} \\ \hat{a}_{\hat{v}} \\ \hat{a}_{\hat{\dot{\sigma}}} \end{bmatrix} - \frac{\Delta t^3}{3!} \begin{bmatrix} \hat{u}\frac{\partial \hat{a}_{\hat{u}}}{\partial x} + \hat{v}\frac{\partial \hat{a}_{\hat{u}}}{\partial y} + \hat{\dot{\sigma}}\frac{\partial \hat{a}_{\hat{u}}}{\partial \sigma} \\ \hat{u}\frac{\partial \hat{a}_{\hat{v}}}{\partial x} + \hat{v}\frac{\partial \hat{a}_{\hat{v}}}{\partial y} + \hat{\dot{\sigma}}\frac{\partial \hat{a}_{\hat{v}}}{\partial \sigma} \\ \hat{u}\frac{\partial \hat{a}_{\hat{\dot{\sigma}}}}{\partial x} + \hat{v}\frac{\partial \hat{a}_{\hat{\dot{\sigma}}}}{\partial y} + \hat{\dot{\sigma}}\frac{\partial \hat{a}_{\hat{\dot{\sigma}}}}{\partial \sigma} \end{bmatrix} \tag{4.8}$$

Here $\mathbf{u} = (u, v, \sigma)$ is determined from (4.5). For evaluating the derivatives in (4.7) and (4.8), second order accurate centered finite differencing on the nonstaggered grid (see section 4.3) is used. The modification of calculation formulas (4.6) to (4.8) for two-dimensional applications is obvious.

4.2.2 Bicubic Lagrange spatial interpolation

Once the departure point has been calculated by the use of a particular D_N scheme for each arrival grid point, the values of variables at the departure points need to be evaluated by means of spatial interpolation from the surrounding grid points. In the present study, bicubic Lagrangian interpolation (e.g. McDonald, 1984) is used for this purpose. Perhaps the most important alternative to bicubic Lagrangian interpolation is cubic spline interpolation. However, semi-Lagrange schemes using cubic spline interpolation is known to be less diffusive at the smallest resolvable scales than schemes using bicubic Lagrangian interpolation (Purnell 1976; Pudykiewicz and Staniforth, 1984; Riishogaard et al., 1998; also see the following discussion for bicubic interpolation). This may lead to the generation of spurious small-scale features. Although the problem may be alleviated by the use of high-order explicit diffusion (Pudykiewicz and Staniforth, 1984; Riishogaard et al., 1998), bicubic Lagrangian interpolation appears to be a safer choice for the interpolation scheme in this study.

In what follows, bicubic Lagrange spatial interpolation is discussed in two spatial dimensions. The main purpose of the discussion is to illuminate the amplitude and phase characteristics of bicubic spatial interpolations. The discussion below can easily be modified to cubic or tricubic interpolation for respective application in one or three spatial dimensions.

The equation describing the two-dimensional advection of a scalar ψ is

$$\frac{D\psi}{Dt} = \frac{\partial \psi}{\partial t} + u\frac{\partial \psi}{\partial x} + v\frac{\partial \psi}{\partial y} = 0, \tag{4.9}$$

where u and v are the horizontal wind components. In a two-dimensional Cartesian coordinate system, let $x = I\Delta x$, $y = J\Delta y$ and $t = n\Delta t$. The semi-Lagrangian discretization of equation (4.9) for the evaluation of ψ at grid point (x, y) is:

$$\psi\left[I\Delta x,\, J\Delta y,\, (n+1)\,\Delta t\right] = \psi\left(x^*,\, y^*,\, n\Delta t\right), \tag{4.10}$$

where (x^*, y^*) is the departure point associated with grid point (x, y). The departure point is calculated with one of the D_N schemes in the present study. In the case of bicubic Lagrange interpolation, the function $\psi(x^*, y^*, t)$ is approximated by a cubic Lagrange interpolating polynomial (Carnahan et al. 1969) using values of ψ at the points nearest to x^* and y^*:

$$\psi(x^*, y^*, t) = \Sigma_\mu \Sigma_\nu W_{\mu\nu} \psi^n_{\mu\nu}. \tag{4.11}$$

Here the notation $\psi^n_{i,j} = \psi(i\Delta x, j\Delta y, n\Delta t)$ was introduced and

$$W_{rs} = \prod_{\mu \neq r} \frac{(x^* - x_\mu)}{(x_r - x_\mu)} \prod_{\nu \neq s} \frac{(y^* - y_\nu)}{(y_s - y_\nu)}. \tag{4.12}$$

The subscripts μ and ν range over the points

$$\mu : i-2, i-1, i, i+1 \qquad \nu : j-2, j-1, j, j+1 \tag{4.13}$$

for the bicubic interpolation scheme. McDonald (1984) showed that if the points (i, j) are chosen such that

$$(i-1)\Delta x < x^* \leq i\Delta x \qquad (j-1)\Delta x < \sigma^* \leq j\Delta\sigma \tag{4.14}$$

the semi-Lagrangian method with bicubic spatial interpolation is unconditionally stable for advection at constant velocity.

Amplitude accuracy

From (4.9), the two-dimensional linear advection equation of a scalar ψ is

$$\frac{D\psi}{Dt} = \frac{\partial\psi}{\partial t} + U\frac{\partial\psi}{\partial x} + V\frac{\partial\psi}{\partial y} = 0, \tag{4.15}$$

where the horizontal wind components U and V are constant in space and time. For the constant velocity field, $D\mathbf{r}^n/Dt = 0$ for $n \geq 2$. From equation (4.1) it follows that all the D_N schemes reduce to the D_1 scheme for a constant velocity field. Applying the D_1 scheme to the case of a constant velocity field, implies that the departure point for each arrival grid point is simply calculated from the formulae:

$$\begin{bmatrix} x^* \\ y^* \end{bmatrix} = \begin{bmatrix} x \\ y \end{bmatrix} - \Delta t \begin{bmatrix} U \\ V \end{bmatrix}. \tag{4.16}$$

The phase and amplitude properties of the semi-Lagrangian method that result when bilinear, biquadratic, bicubic and biquartic interpolation schemes are applied to calculate the value of variables at the departure point calculated by (4.16), have been analysed by McDonald (1984). In order to aid the interpretation of numerical results in Chapter 5, the results of McDonald (1984) are reviewed in this and the following section for the bicubic interpolation scheme. The amplitude accuracy of the semi-Lagrangian method may be analysed by using the von Neumann method (e.g. Richtmeyer and Morton, 1967; Mesinger and Arakawa, 1976). To this end, define α, β, $\hat{\alpha}$ and $\hat{\beta}$ as:

$$\alpha = u\frac{\Delta t}{\Delta x} \qquad \beta = v\frac{\Delta t}{\Delta y} \tag{4.17}$$

$$\hat{\alpha} = \alpha + i - I \qquad \hat{\beta} = \beta + j - J. \tag{4.18}$$

α and β may be termed the x and y direction Courant numbers respectively. The selection of interpolation points i and j according to (4.14) guarantees that

$$0 \leq \hat{\alpha} < 1, \qquad 0 \leq \hat{\beta} < 1. \tag{4.19}$$

These are sufficient conditions to ensure absolute stability of the semi-Lagrangian scheme when applied to the linear advection equation (McDonald, 1984). This may be shown by substituting wave-like solutions of the form

$$\psi^n_{I,\,J} = \psi_0 \lambda^n \exp^{i_c(kI\Delta x + lJ\Delta y)} \tag{4.20}$$

into equation (4.10). Here $i_c^2 = -1$; $k = 2\pi/L_x$and $l = 2\pi/L_y$ with L_x and L_y the wave lengths in the x and y directions respectively. λ is the amplification factor. Using (4.14) to evaluate $\psi\left(x^*,\, y^*,\, n\Delta t\right)$, shows that λ splits into an "x amplification factor" and "y amplification factor" as follows (McDonald, 1984):

$$\lambda = \hat{\Lambda}\left(\hat{\alpha},\, k\right)\hat{\Lambda}\left(\hat{\beta},\, l\right). \tag{4.21}$$

Here

$$\left|\hat{\Lambda}\left(\hat{\alpha},\, k\right)\right|^2 = 1 - \hat{\alpha}\left(2 - \hat{\alpha}\right)\left(1 - \hat{\alpha}^2\right)c^2\left[3 + 2c\hat{\alpha}\left(1 - \hat{\alpha}\right)\right]\frac{1}{9}, \tag{4.22}$$

where $c = 1 - \cos k\Delta x$. The formula for $\left|\hat{\Lambda}\left(\hat{\beta},\, l\right)\right|^2$ is given by (4.22) with $\hat{\alpha}$ replaced by $\hat{\beta}$ and k replaced by l. The lines of constant $\left|\Lambda\left(\hat{\alpha},\, k\right)\right|$ are displayed in Fig.4.1 for $0 \leq k\Delta x/\pi \leq 1$ and $0 \leq \alpha \leq 1$. (Note that the shortest waves that may be reolved on the nonstaggered grid with constant grid interval Δx have wave length $2\Delta x$. Thus, $2\Delta x \leq L_x <\leq \infty$, which implies that $0 < k\Delta x \leq \pi$.)

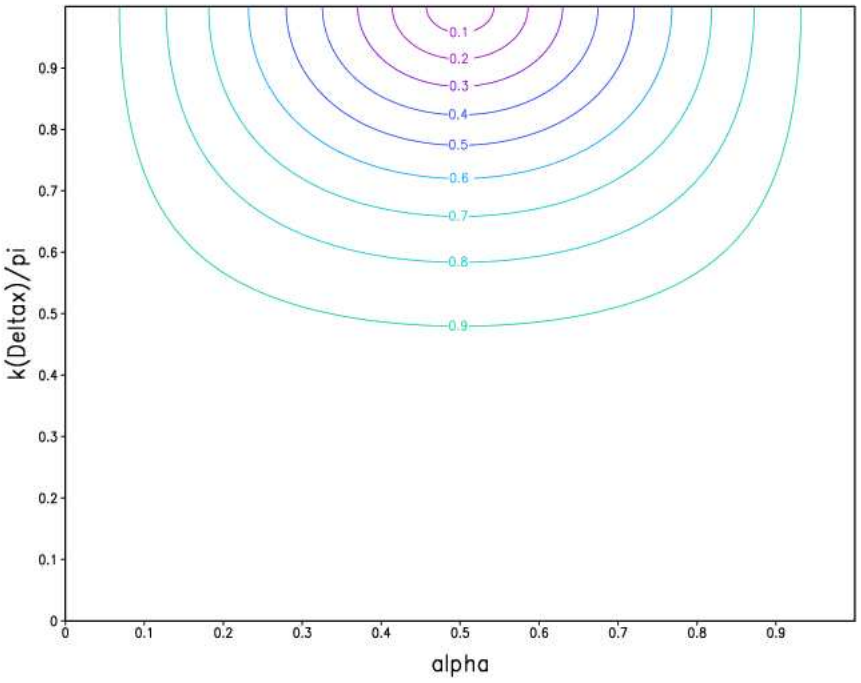

Figure 4.1: Isolines of the amplification factor for bicubic spatial interpolation, as a function of α and $k\Delta x/\pi$ (following McDonald, 1984).

From Fig. 4.1 it can be seen that the bicubic interpolation scheme results in the most severe damping of the scalar ψ when $\alpha = 0.5$. The scheme is undamped for $\alpha = 0$ or 1. The damping is the heaviest for the shortest resolvable wave lengths, and it decreases as the wave length increases (McDonald, 1984). At the shortest resolvable scales, numerical solution of the nonlinear advection equation may result in aliasing errors (where waves of length smaller than two grid intervals are spuriously represented as waves longer than two grid lengths (see Mesinger and Arakawa, 1976). The severe damping of the shortest resolvable wave lengths may be regarded as an advantage of the bicubic Lagrange interpolation scheme, as it funtions to control the numerical "noise" that may be originating at these scales.

Phase accuracy

Another important measure of accuracy of a numerical advection scheme, is how the phase speed of the numerical solution of the advection equation compares to that of the true solution. The phase speed analysis is usually performed in one spatial dimension, since a two-dimensional analysis is cumbersome to perform and the result can not be easily quantitatively interpreted or graphically displayed. Note that for the linear one-dimensional advection equation, the phase speed of the true solution is $\Upsilon = -ku\Delta t$ (Mesinger and Arakawa, 1976), whilst the phase speed of the numerical solution is given by $\tan^{-1}(\lambda_{im}/\lambda_{re})$. Here λ_{im} and λ_{re} are respectively the real and imaginary parts of the amplification factor λ (see Mesinger and Arakawa, 1976). The relative phase speed is therefore defined as

$$R_A = \frac{1}{\Upsilon} \tan^{-1} \frac{\lambda_{im}}{\lambda_{ir}}.$$

The relative phase speed R_A normalised to u of the bicubic Lagrange interpolation scheme, when applied to one dimensional linear advection, is (McDonald, 1984):

$$R_{AL}(\alpha,\, k) = \frac{p}{\alpha} + \frac{\hat{\alpha} \sin k\Delta x \left[1 + a\left(1 - \hat{\alpha^2}\right)/3\right]}{\left(1 - a\hat{\alpha^2} - a^2\alpha\left(1 - \hat{\alpha^2}\right)/3\right)}.$$

The relative phase speed R_A is displayed in Fig. 4.2 as a function of α and k.

It may be seen from Fig. 4.2 that the phase errors decrease as the wave length increases, for all α. Close to $\alpha = 0$ the phase errors is the largest, whereas the error is zero at $\alpha = 1$. Thus, the bicubic interpolation scheme gives a faithful representation of both amplitude and phase of the true solution at large Courant numbers (close to 1). In fact, similar amplitude and phase properties are valid in the region around $\alpha = 2$ (see McDonald, 1984). This implies that a semi-Lagrangian model may be applied at large Courant numbers (large time steps),

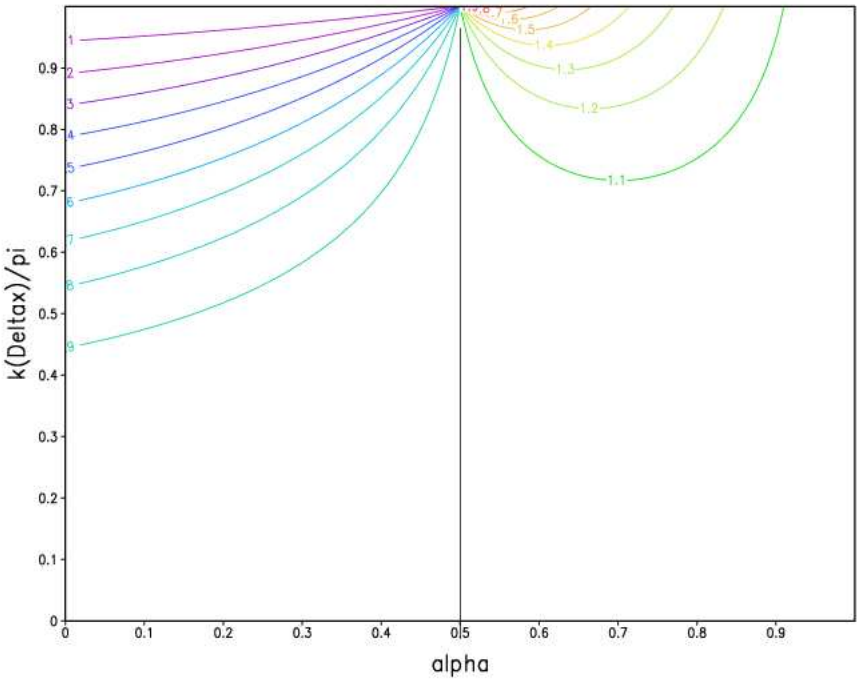

Figure 4.2: Normalised phase speed isolines for bicubic spatial interpolation, as a function of α and $k\Delta x/\pi$ (following McDonald, 1984).

which is advantageous from a computational perspective, without compromising the accuracy of the scheme with respect to amplitude and phase characteristics.

4.3 Finite differencing on the nonstaggered grid

Centered differencing formulae for collinear data were derived by Purser and Leslie (1988), by fitting Lagrange interpolation polynomials appropriate to centered differencing to the relevant number of data points. In this section, these centered differencing formulae of various orders of accuracy are stated for application on the nonstaggered grid. The formulae are then applied to pure gravity wave equations, in order to examine the frequency response of the waves to spatial discretization on the nonstaggered grid. This analysis is of use in section 4.8, where the response of the split semi-Lagrangian scheme to spatial discretization on the nonstaggered grid is examined.

The data are assumed to be positioned at integer multiples of a constant grid space d, that is,

$$a_i = a(id). \tag{4.23}$$

It is convenient to define the binomial envelope function (Purser and Leslie, 1988) $\beta_{M,j}$ as:

$$\beta_{M,j} = \frac{(M!)^2}{(M+j)!\,(M-j)!}. \tag{4.24}$$

4.3.1 Centered differencing for first derivatives

The centered differencing formulae (of even order $2M$) for first derivatives can be expressed as (Purser and Leslie, 1988):

$$\frac{da}{dx}|_{x=id} \approx \frac{1}{d}\Sigma_{j=-M}^{M} D_{M,j} a_{i+j}, \tag{4.25}$$

where

$$D_{M,j} = -D_{M,-j}, \tag{4.26}$$

and

$$D_{M,j} = -\frac{(-1)^j}{j}\beta_{M,j}, \quad j = \pm 1, \ldots \pm M. \tag{4.27}$$

From (4.24) to (4.26) with $M = 1$ the usual centered differencing formula of second order accuracy for first derivatives follows:

$$\frac{da}{dx}|_{x=id} \approx \frac{1}{2d}\left(a_{i+1} - a_{i-1}\right). \tag{4.28}$$

$M = 2$ gives a formula of fourth order accuracy

$$\frac{da}{dx}|_{x=id} = \frac{1}{d}\left(\frac{1}{12}a_{i-2} - \frac{2}{3}a_{i-1} + \frac{2}{3}a_{i+1} - \frac{1}{12}a_{i+2}\right), \tag{4.29}$$

whilst $M = 3$ implies a formula of sixth order accuracy

$$\frac{da}{dx}|_{x=id} = \frac{1}{d}\left(-\frac{1}{60}a_{i-3} + \frac{3}{20}a_{i-2} - \frac{3}{4}a_{i-1} + \frac{3}{4}a_{i+1} - \frac{3}{20}a_{i+2} + \frac{1}{60}a_{i+3}\right). \tag{4.30}$$

4.3.2 Centered differencing for second derivatives

The centered nonstaggered formula for second derivatives from $2M + 1$ points is (Purser and Leslie, 1988):

$$\frac{d^2a}{dx^2}|_{x=id} \approx \frac{1}{d^2}\Sigma_{j=-M}^{j=M} D_{M,j}^{(2)} a_{i+j}, \tag{4.31}$$

where

$$D_{M,j}^{(2)} = D_{M,-j}^{(2)}, \tag{4.32}$$

and

$$D_{M,j}^{(2)} = \frac{-(-1)^j}{j^2} 2\beta_{M,j}, \quad j = \pm 1, \ldots \pm M, \tag{4.33}$$

with

$$D_{M,0}^{(2)} = -\Sigma_{j\neq 0} D_{M,j}^{(2)}. \tag{4.34}$$

From (4.24) and (4.31) to (4.34) with $M = 1$ the usual centered differencing formula of second order accuracy for second derivatives follows:

$$\frac{d^2a}{dx^2} \approx \frac{1}{d^2}\left(a_{i-1} - 2a_i + a_{i+1}\right) \tag{4.35}$$

$M = 2$ gives a formula of fourth order accuracy

$$\frac{d^2a}{dx^2} \approx \frac{1}{d^2}\left(-\frac{1}{12}a_{i-2} + \frac{4}{3}a_{i-1} - \frac{5}{2}a_i + \frac{4}{3}a_{i+1} - \frac{1}{12}a_{i+2}\right), \tag{4.36}$$

whilst $M = 6$ implies a formula of sixth order accuracy

$$\frac{d^2a}{dx^2} \approx \frac{1}{d^2}\left(\frac{1}{90}a_{i-3} - \frac{3}{20}a_{i-2} + \frac{3}{2}a_{i-1} - \frac{49}{18}a_i + \frac{3}{2}a_{i+1} - \frac{3}{20}a_{i+2} + \frac{1}{90}a_{i-3}\right). \tag{4.37}$$

4.3.3 Application to one-dimensional gravity waves

In the equations that govern the simple case of pure gravity waves (see Mesinger and Arakawa, 1976), the dependent variables are functions of one space variable only. The pure gravity wave equations are

$$\frac{\partial u}{\partial t} = -g\frac{\partial h}{\partial x}, \quad \frac{\partial h}{\partial t} = -H\frac{\partial u}{\partial x}; \tag{4.38}$$

with g (gravitational acceleration) and H (the mean depth of the fluid) constants. u is the horizontal wind and h the depth of the fluid. These equations are sometimes referred to as the shallow-water equations (e.g. Holton, 1992), although this terminology has been applied more generally to describe the system of gravity-inertia waves (e.g. McGregor, 2005). Following Mesinger and Arakawa (1976), wave solutions of the form

$$Q\left(x,\, t\right) = \hat{Q}\exp^{i_c(kx-\Omega_T)} \tag{4.39}$$

are substituted in (4.38), which leads to the homogeneous system

$$\Omega_T\hat{u} = gk\hat{h}, \quad \Omega_T\hat{h} = Hk\hat{u}. \tag{4.40}$$

Here $\Omega_T = kc$, where k is the horizontal wave number and c is the phase speed of the gravity waves. Equations (4.40) imply the frequency equation

$$\Omega_T^2 = gHk^2, \tag{4.41}$$

or alternatively,

$$c = \frac{\Omega_T}{k} = \pm\sqrt{gH}. \tag{4.42}$$

Thus, the gravity waves propagate along the x axis in both directions at a constant speed $\sqrt{gH}$, irresepective of the wave length of the waves.

Mesinger and Arakawa (1976) analysed the gravity wave response of (4.38) to second order spatial discretization on the nonstaggered grid. Their discussion is repeated in the the next section, followed by a discussion for higher-order differentiation on the nonstaggered grid in sections 4.3.3.2 and 4.3.3.3.

4.3.3.1 Second order spatial differencing

When the space derivatives in (4.38) are approximated by second order centered differencing, the differential-difference equations

$$\frac{\partial u_i}{\partial t} = -g\frac{h_{i+1}-h_{i-1}}{2\Delta x}, \quad \frac{\partial h_i}{\partial t} = -H\frac{u_{i+1}-u_{i-1}}{2\Delta x} \tag{4.43}$$

are obtained. Here Δx denotes the constant grid space d in (4.23). The solutions (4.39) now assume the form

$$Q_i(t) = \hat{Q} \exp^{i_c(ki\Delta x - \Omega_N t)}, \tag{4.44}$$

where Ω_N denotes the frequency of the gravity waves in the numerical solution. Substitution of (4.44) into (4.43) leads to

$$\Omega_N \hat{u} = g\frac{\sin k\Delta x}{\Delta x}, \quad \Omega_N \hat{h} = H\frac{\sin k\Delta x}{\Delta x}\hat{u}, \tag{4.45}$$

giving the frequency equation

$$\Omega_N^2 = gH\left(\frac{\sin k\Delta x}{\Delta x}\right)^2. \tag{4.46}$$

The relative frequency of gravity waves in the numerical solution (compared to that of the true solution) obtained with second order spatial differencing may be defined as

$$R_2 = \frac{\Omega_T}{\Omega_N} = \frac{\sin k\Delta x}{k\Delta x}. \tag{4.47}$$

Thus, it may be noted that instead of a constant phase speed, the gravity waves now propagate with the phase speed

$$c_2 = \pm\sqrt{gH}\frac{\sin k\Delta x}{k\Delta x}, \tag{4.48}$$

or alternatively,

$$c_2 = cR_2. \tag{4.49}$$

The phase speed of gravity waves c_2 in the numerical solution is not a constant like the true phase speed, but depends on the wave number. Thus, the centered space differencing results in computational dispersion. The relative frequency R_2 is shown in Fig. 4.3 as a function of the normalized wave number $k\Delta x/\pi$ (black line). The $2\Delta x$ wave is stationary. For wave lengths equal to $4\Delta x$, that is, for $k\Delta x/\pi = 1/2$, the relative frequency is about 60%. Thus, there is a significant retardation of the true gravity wave phase speed near the shortest resolvable scales. However, the relative frequency of the waves increases as the wave length increases, and the numerical frequency approach the true frequency in the long wave limit (Fig. 4.3).

4.3.3.2 Fourth order spatial differencing

When the space derivatives in (4.38) are approximated with fourth order centered differences, the differential-difference equations

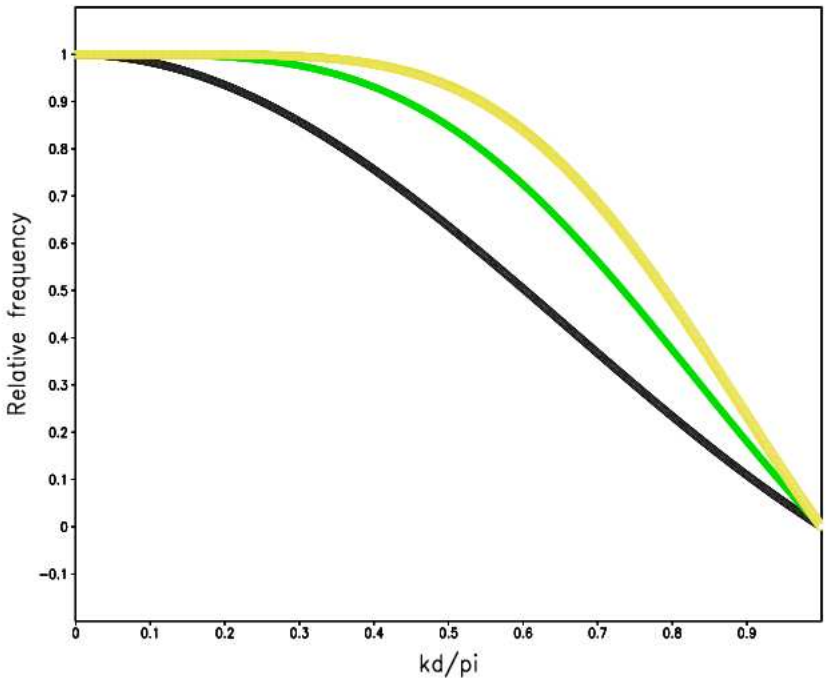

Figure 4.3: The relative frequency of pure gravity waves as a function of wave number, for second order (black line), fourth order (green line) and sixth order (yellow line) spatial differencing on the nonstaggered grid.

$$\frac{\partial u_i}{\partial t} = -\frac{g}{\Delta x}\left(\frac{1}{12}h_{i-2} - \frac{2}{3}h_{i-1} + \frac{2}{3}h_{i+1} - \frac{1}{12}h_{i+2}\right),$$

$$\frac{\partial h_i}{\partial t} = -\frac{H}{\Delta x}\left(\frac{1}{12}u_{i-2} - \frac{2}{3}u_{i-1} + \frac{2}{3}u_{i+1} - \frac{1}{12}u_{i+2}\right). \tag{4.50}$$

are obtained. Substitution of (4.44) into (4.50) leads to

$$\Omega_N \hat{u} = \frac{g}{\Delta x}\left(\frac{4}{3}\sin k\Delta x - \frac{1}{6}\sin 2k\Delta x\right)\hat{h},$$

$$\Omega_N \hat{h} = \frac{H}{\Delta x}\left(\frac{4}{3}\sin k\Delta x - \frac{1}{6}\sin 2k\Delta x\right)\hat{u}, \tag{4.51}$$

giving the frequency equation

$$\Omega_N^2 = \frac{gH}{\Delta x^2}\left(\frac{4}{3}\sin k\Delta x - \frac{1}{6}\sin 2k\Delta x\right)^2. \tag{4.52}$$

The relative frequency of gravity waves in the numerical solution obtained with fourth order spatial differencing therefore is

$$R_4 = \frac{\Omega_T}{\Omega_N} = \frac{1}{k\Delta x}\left(\frac{4}{3}\sin k\Delta x - \frac{1}{6}\sin 2k\Delta x\right). \tag{4.53}$$

Thus, the gravity waves in the numerical solution propagate with the phase speed

$$c_4 = \pm\sqrt{gH}\frac{1}{k\Delta x}\left(\frac{4}{3}\sin k\Delta x - \frac{1}{6}\sin 2k\Delta x\right), \tag{4.54}$$

or alternatively,

$$c_4 = cR_4. \tag{4.55}$$

The relative frequency R_4 is shown in Fig. 4.3 as a function of the normalized wave number $k\Delta x/\pi$ (green line).

4.3.3.3 Sixth order spatial differencing

When the space derivatives in (4.38) are approximated by sixth order centered differences, the differential-difference equations

$$\frac{\partial u_i}{\partial t} = -\frac{g}{\Delta x}\left(-\frac{1}{60}h_{i-3} + \frac{3}{20}h_{i-2} - \frac{3}{4}h_{i-1} + \frac{3}{4}h_{i+1} - \frac{3}{20}h_{i+2} + \frac{1}{60}h_{i+3}\right),$$

$$\frac{\partial h_i}{\partial t} = -\frac{H}{\Delta x}\left(-\frac{1}{60}u_{i-3} + \frac{3}{20}u_{i-2} - \frac{3}{4}u_{i-1} + \frac{3}{4}u_{i+1} - \frac{3}{20}u_{i+2} + \frac{1}{60}u_{i+3}\right), \tag{4.56}$$

result. Substitution of (4.44) into (4.50) leads to

$$\Omega_N \hat{u} = \frac{g}{\Delta x}\left(\frac{3}{2}\sin k\Delta x - \frac{3}{10}\sin 2k\Delta x + \frac{1}{30}\sin 3k\Delta x\right)\hat{h},$$

$$\Omega_N \hat{h} = \frac{H}{\Delta x}\left(\frac{3}{2}\sin k\Delta x - \frac{3}{10}\sin 2k\Delta x + \frac{1}{30}\sin 3k\Delta x\right)\hat{u}. \tag{4.57}$$

giving the frequency equation

$$\Omega_N^2 = \frac{gH}{\Delta x^2}\left(\frac{3}{2}\sin k\Delta x - \frac{3}{10}\sin 2k\Delta x + \frac{1}{30}\sin 3k\Delta x\right)^2. \tag{4.58}$$

The magnitude of relative frequency of gravity waves in the numerical solution obtained with sixth order spatial differencing therefore is

$$R_6 = \frac{\Omega_T}{\Omega_N} = \frac{1}{k\Delta x}\left(\frac{3}{2}\sin k\Delta x - \frac{3}{10}\sin 2k\Delta x + \frac{1}{30}\sin 3k\Delta x\right). \tag{4.59}$$

Thus, the gravity waves in the numerical solution propagate with the phase speed

$$c_6 = \pm\sqrt{gH}\frac{1}{k\Delta x}\left(\frac{3}{2}\sin k\Delta x - \frac{3}{10}\sin 2k\Delta x + \frac{1}{30}\sin 3k\Delta x\right), \tag{4.60}$$

or alternatively,

$$c_6 = cR_6. \tag{4.61}$$

The relative frequency R_6 is shown in Fig. 4.3 as a function of the normalized wave number $k\Delta x/\pi$ (yellow line). Comparing the relative frequency at fourth and sixth-order to the second-order result reveals a great improvement for the scales

$$k\Delta x/\pi < 1/2. \tag{4.62}$$

These are the waves with wave lengths larger than $4\Delta x$. The relative frequency for a wave of length $4\Delta x$ is about 88% at fourth-order, and 92% at the sixth-order, compared to 60% at second-order. Thus, at sixth-order differencing the error in the numerical frequency is less than 10% for the important range (4.62). Similar results were obtained for the shallow-water equations by Purser and Leslie (1988). More insight into the improvement gained in the relative frequency can be obtained by considering Fig. 4.4. Here the relative frequency is plotted for second-order (black), fourth-order (green) and sixth-order (yellow) differencing as a function of the horizontal wave length, for $200\,m \leq L_x \leq 1000\,m$. In the relevant formulas of relative frequency (4.47), (4.53) and (4.59), $\Delta x = 100\,m$ is used, implying that the shortest resolvable wave has wave length $200\,m$. The red line in Fig. 4.4 is obtained from using

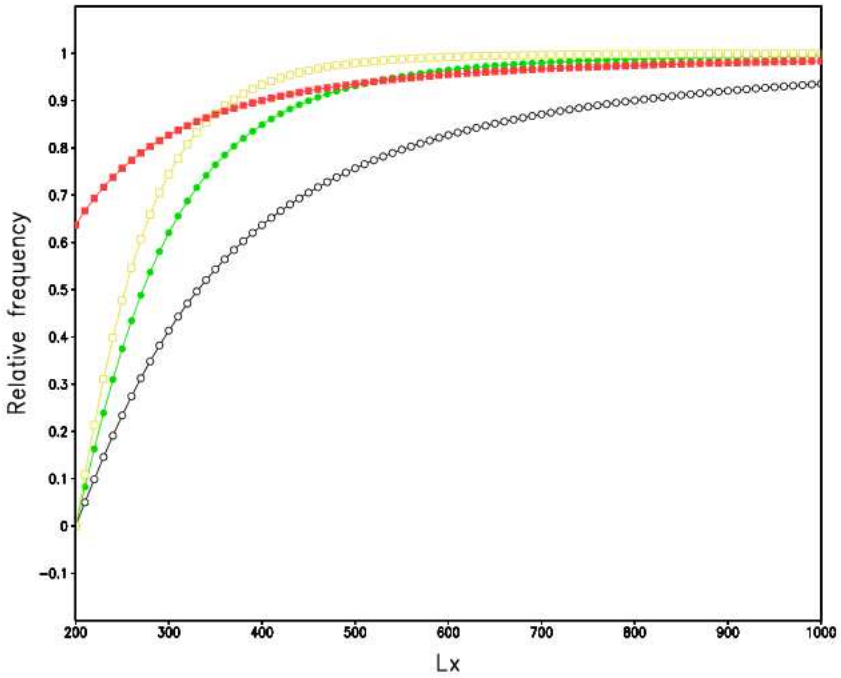

Figure 4.4: The relative frequency of pure gravity waves as a function of wave length, for second order (black line), fourth order (green line) and sixth order (yellow line) spatial differencing on the nonstaggered grid with $\Delta x = 100\,m$. The red line represents the relative frequency of pure gravity waves for second order differencing on the nonstaggered grid with $\Delta x = 50\,m$.

$\Delta x = 50m$ in the relative frequency formula (4.47) obtained with second-order differencing. The doubling of grid resolution results in a far more accurate representation of the frequency of the short wave length gravity waves for second-order differencing (note, however, that the $2\Delta x = 100\,m$ wave is stationary for the case $\Delta x = 50\,m$). It can also be seen in Fig. 4.4 that fourth and sixth-order differencing at a specific grid length produces more accurate results than second-order differencing at double the resolution, for waves lengths larger than about 1.5 and 2.5 grid-lengths respectively. However, despite the advantages to be gained from higher-order differencing at short wave lenghts, the presence of stationary $2\Delta x$ waves remain problematic, irrespective of the degree of the order of differencing.

4.4 Spatial filtering

The unpopularity of the nonstaggered grid in meteorological modelling is largely due to the presence of the spurious stationary two-grid-interval waves, that appear as solutions of the pure gravity wave equations in response to spatial discretization on this grid. When the Coriolis terms are also present, the two-grid-interval waves appear with false low frequencies as pure inertia waves (Mesinger and Arakawa, 1976).

Shapiro (1975) devised a family of stable filters that remove completely the two-grid-interval waves. These filters affect the asymptotically long waves to the least extent possible given the width of each filter's stencil (Purser, 1987).

The one-dimensional filtering operator proposed by Shapiro (1976) for a variable f on a nonstaggered grid is

$$f_i^{p+1} = 1 - \frac{1}{2^{2p+2}} \begin{pmatrix} 2p & +2 \\ p & +1 \end{pmatrix} f_i$$

$$+ \left[\frac{(-1)^p}{2^{2p+2}}\right] \Sigma_{j=0}^{p} (-1)^j \begin{pmatrix} 2p+2 \\ j \end{pmatrix} \left[f_{i+(1+p-j)} + f_{i-(1+p-j)}\right], \qquad (4.63)$$

where $\begin{pmatrix} n \\ m \end{pmatrix} = n!/\left[(n-m)!m!\right]$. The amplitude response function for the operator (4.63) is

$$AR = 1 - \sin^{2p+2}\alpha. \qquad (4.64)$$

Here $\alpha = n\Delta x/2$; $n = 2\pi/\lambda$ with λ the wave length of the component.

In the numerical experiments performed in Chapter 5, $p = 4$ was found to produce satisfactory results. In this case the filtering operator is

$$f_i^5 = \frac{1}{2^{10}}\left[f_{i-5} - 10f_{i-4} + 45f_{i-3} - 120f_{i-2} + 210f_{i-1} + 772f_i\right.$$

$$\left. +210f_{i+1} - 120f_{i+2} + 45f_{i+3} - 10f_{i+4} + f_{i+5}\right] \tag{4.65}$$

For the operator (4.65) the amplitude response of the three-grid, four-grid and six-grid-interval waves are 0.76270, 0.96875 and 0.99902 respectively (Shapiro, 1975). This illustrates the mimimal effect that the filter has at longer wave lengths. Thus, the high-order Shapiro filter is a highly scale-dependent explicit smoothing operator. Its application in the split semi-Lagrangian scheme is discussed in section 4.5.3.

4.5 The split semi-Lagrangian solution procedure

In this section, a two time-level, time-split, semi-Lagrangian scheme is constructed for solving the σ coordinate quasi-elastic equations (3.64) to (3.68). The solution procedure is split into four different phases. The first phase is a semi-Lagrangian advection step with time step Δt_s, followed by an adjustment procedure with N adjustment steps each having time step $\Delta t_a = \Delta t_s/N$. The third and fourth phases consist of the application of a highly scale-dependent spatial filter and explicit diffusion respectively. The horizontal and vertical differencing are carried out on a nonstaggered grid.

4.5.1 Splitting off the advective part

Suppose that the values of all seven variables u, v, $\Omega = \omega/p$, $\dot{\sigma}$, T, ϕ and p_s are known at time level t. The advection process in the horizontal momentum, continuity and thermodynamic energy equations is represented by the following equations:

$$\frac{Du}{Dt} = 0, \tag{4.66}$$

$$\frac{Dv}{Dt} = 0, \tag{4.67}$$

$$\frac{D\ln p_s}{Dt} = 0, \tag{4.68}$$

$$\frac{DT}{Dt} = 0. \tag{4.69}$$

The semi-Lagrangian approach is used to calculate the contribution of advection to the fields u, v, $\ln p_s$ and T at the arrival points . One of the the D_N schemes of McGregor (1993) is applied in three spatial dimensions to calculate the time-level t departure points (x^*, y^*, σ^*) for each time-level $t+\Delta t_s$ arrival grid point. Note that the values of u, v and $\dot{\sigma}$ are required at time levels t, $t-\Delta t$ and $t-2\Delta t$ in order to evaluate (4.5) for application in the D_N scheme. The values of u, v, $\ln p_s$ and T are evaluated at the departure points using a tricubic extension of the bicubic interpolation scheme presented in section 4.2.2 to three spatial dimensions. Note that for application in two spatial dimensions, a D_N scheme is used with bicubic spatial interpolation as discussed in section 4.2.2. Let the departure point values of u, v, $\ln p_s$ and T obtained from the semi-Lagrangian procedure be denoted by u^*, v^*, $\ln p_s^*$ and T^*.

An important feature of the scheme is the use of (4.68) by means of the calculation of the quantity $\ln p_s$ at time level $t+\Delta t_s$ from the semi-Lagrangian procedure, at each arrival grid point. At the end of the advection step, the quantity $A_{p_s} = -u\,(\partial \ln p_s/\partial x) - v\,(\partial \ln p_s/\partial y)$ at time level $t+\Delta t_s$ is diagnosed at each arrival grid point, for use in the adjustment phase of the solution procedure. That is, the the term is effectively calculated from the values of u^*, v^* and $\ln p_s^*$ that correspond to each arrival grid point and it represents the change in the local time tendency of $\ln p_s$ because of advection. Therefore, let this field be denoted by $A_{p_s}^*$. Alternatively, the quantity A_{p_s} may be diagnosed at the beginning of each time step for each grid point and the departure point values ($A_{p_s}^*$) calculated from the semi-Lagrangian procedure for each arrival grid point. The value of $\ln p_s^*$ may then be obtained from $A_{p_s}^*$. The latter approach was followed by McGregor (1986) and Leslie and Purser (1991) to solve hydrostatic equation sets. The numerical experiments performed in Chapter 5 indicate that these two approaches of calculating the advective change to the surface pressure give almost indistinguishable results. Note that a semi-Lagrangian discretization of the vertical momentum equation is not employed in the scheme.

4.5.2 The adjustment step

The values u^*, v^* and T^* calculated during the advection step for each arrival grid point, are used as initial values for the fields of u, v and T during the first step of the adjustment phase of the solution procedure. Initial values required for the fields p_s, ω/p and ϕ, are taken to be effectively at time level t. Forward differences in time are used to update the fields of u, v at time level $t+\Delta t_a$:

$$\frac{u^{t+k\Delta t_a} - u^{t+(k-1)\Delta t_a}}{\Delta t_a} = \left(-\frac{\partial \phi}{\partial x} + \sigma \frac{\partial \phi}{\partial \sigma}\frac{\partial \ln p_s}{\partial x} \right)^{t+(k-1)\Delta t_a} + \frac{f}{2}\left(v^{t+(k-1)\Delta t_a} + v^{t+k\Delta t_a} \right), \tag{4.70}$$

$$\frac{v^{t+k\Delta t_a} - v^{t+(k-1)\Delta t_a}}{\Delta t_a} = \left(-\frac{\partial \phi}{\partial y} + \sigma \frac{\partial \phi}{\partial \sigma}\frac{\partial \ln p_s}{\partial y}\right)^{t+(k-1)\Delta t_a} - \frac{f}{2}\left(u^{t+(k-1)\Delta t} + u^{t+k\Delta t}\right), \tag{4.71}$$

Here k ranges from 1 to N. Note that trapezoidal time stepping (Fisher, 1965; Janjic and Wiin-Nielsen, 1977) is used to treat the Coriolis terms semi-implicitly. The surface pressure tendency $\partial \ln p_s/\partial t$ at time level $t+k\Delta t_a$ is diagnosed using the latest values of u and v, with backward time differencing being applied to update $\ln p_s$ (and thence p_s):

$$\frac{\ln p_s^{t+k\Delta t_a} - \ln p_s^{t+(k-1)\Delta t_a}}{\Delta t_a} = \int_0^1 \left[A^*_{p_s} - \left(\frac{\partial u}{\partial x} + \frac{\partial v}{\partial y}\right)^{t+k\Delta t_a}\right] d\sigma \tag{4.72}$$

Note that (4.72) is obtained from integrating (3.67) over σ, from the model top $\sigma = 0$ to the surface $\sigma = 1$. The field $A^*_{p_s}$ is assumed to remain constant during the adjustment phase. Experiments were performed in which A_{p_s} was updated at the end of each adjustment time step using the latest values of u, v and p_s, but this had an insignificant effect on the simulations. In fact, the contribution of term A_{p_s} to (4.72) and (4.73) was found to be insignificant in the numerical experiments described in the next section. However, these experiments were performed for the case of zero topography; it is likely that the term is more important in regions of steep terrain. The fields of $\dot{\sigma}$ and ω/p are diagnosed consistently with the field $\partial \ln p_s/\partial t$ at time level $t + k\Delta t_a$:

$$\dot{\sigma}^{t+k\Delta t_a} = -\sigma\left(\frac{\partial \ln p_s}{\partial t}\right)^{t+k\Delta t_a} + \int_0^\sigma \left[A^*_{p_s} - \left(\frac{\partial u}{\partial x} + \frac{\partial v}{\partial y}\right)^{t+k\Delta t_a}\right] d\sigma', \tag{4.73}$$

$$\left(\frac{\omega}{p}\right)^{t+k\Delta t_a} = \left\{\frac{p_s^{t+k\Delta t_a}}{\sigma p_s^{t+k\Delta t_a} + p_T}\left\{\sigma\left[\left(\frac{\partial \ln p_s}{\partial t}\right)^{t+k\Delta t_a} - A^*_{p_s}\right] + \dot{\sigma}^{t+k\Delta t_a}\right\}\right\}. \tag{4.74}$$

Here (4.73) has been obtained by integrating (3.67) in the vertical from the model top to level σ and (4.74) follows from relationship (3.69). The temperature field T may now be updated using backward time differencing

$$\frac{T^{t+k\Delta t_a} - T^{t+(k-1)\Delta t_a}}{\Delta t_a} = \kappa\left(\frac{\omega}{p}\right)^{t+k\Delta t_a} T^{t+k\Delta t_a}. \tag{4.75}$$

It is interesting to note that in the semi-implicit solution of the hydrostatic equations used in C-CAM, the right-hand side of the thermodynamic equation (4.75) is handled implicitly with regard to ω. This is necessary because of gravity wave feedback into the ϕ terms of the horizontal momentum equations (McGregor, personal communication). In the present approach this treatment is avoided by diagnosing ϕ from the elliptic equation (see the next paragraph).

Finally, the geopotential field at time-level $t + k\Delta t_a$ is diagnosed from the discretized version of the elliptic equation (3.81). This equation is solved iteratively, using Successive Over-Relaxation (SOR). In most of the numerical experiments performed in Chapter 5, only a few interations are required to obtain suitable convergence of the solution. The iterative solution procedure is outlined in some detail in section 4.6, whilst the computational efficiency of the elliptic solver is discussed in more detail in Chapter 5. It may be noted that the vertical momentum equation is never used explicitly in the solution procedure, but is implicitly present in (3.81).

4.5.3 Spatial filtering

After both the advection step and the N adjustment steps have been performed, spatial filtering is applied to some of the variables calculated. The Shapiro (1975) filter discussed in section 4.4 is applied to perform spatial filtering of the fields u, v, p_s, $\dot{\sigma}$ and ϕ. Since the variable ω/p is diagnosed from the (filtered) fields of $\ln p_s$ and $\dot{\sigma}$ in the adjustment procedure, without any additional centered differencing being performed, there is no need to perform filtering on this field. It is also essential that the spatial filter is not applied to the temperature field. This is due to the fact that no spatial derivatives occur in the adjustment step equation (4.75), which is used to update the temperature field (see section 4.5.2). By the time that the temperature field is updated in the adjustment phase procedure, the right-hand side of (4.75) is effectively already filtered (the spatial filter is applied to p_s and $\dot{\sigma}$ used to diagnose ω/p in (4.75)). It is not meaningful to apply the spatial filter to an already filtered field. Numerical simulations (see Chapter 5) where the temperature field is filtered show excessive numerical noise. Numerical experiments indicated that generally filtering with $p = 4$ produces satisfactory results (see Chapter 5). The horizontal filtering is first performed in the x direction

$$f^5_{i,\,j} = \frac{1}{2^{10}}\left[f_{i-5,\,j,\,k} - 10f_{i-4,\,j,\,k}, +45f_{i-3,\,j,\,k} - 120f_{i-2,\,j,\,k} + 210f_{i-1,\,j,\,k} + \right.$$

$$\left. 772f_{i,\,j,\,k} + 210f_{i+1,\,j,\,k} - 120f_{i+2,\,j,\,k} + 45f_{i+3,\,j,\,k} - 10f_{i+4,\,j,\,k} + f_{i+5,\,j,\,k}\right], \tag{4.76}$$

for each variable u, v, p_s,$\dot{\sigma}$, T and ϕ. This is followed by similar filtering in the y and σ directions.

The spatial filtering effectively removes the two-grid-interval waves from the nonstaggered grid (Shapiro, 1975; also see section 4.4 and Chapter 5), whilst the damping at longer wave lengths is sufficiently small not to impact negatively on the simulations (see section 4.4 and Chapter 5). Thus, the spatial filtering provides highly scale-dependent, explicit filtering in the model. The split semi-Lagrangian scheme with application of the Shapiro filter is stable at large Courant numbers (see Chapter 5).

4.5.4 Explicit diffusion

After application of the Shapiro filter, there is no need to apply explicit diffusion (smoothing) in the split semi-Lagrangian scheme in order to ensure numerical stability, or to control numerical noise originating from the nonstaggered grid. However, the use of explicit diffusion may still be useful in order to obtain a grid-converged solution of a specific flow problem (Straka et al., 1993). In the absence of explicit diffusion, an increase in model resolution will always result in smaller scales of motion to be resolved. However, by applying explicit diffusion, a limit is placed in the resolvable scales, so that numerical solutions of a given flow problem will converge towards a so called "grid converged solution" at increasing resolution. Grid-converged solutions of specific flow problems are most useful for the comparison of different numerical schemes to each other, and to study the characteristics of a specific numerical scheme. In Chapter 5, the simulation of warm and cold convective bubbles by the split semi-Lagrangian scheme are compared to well-known grid-converged solutions of these problems. Thus, after application of the Shapiro filter, explicit filtering is applied in a split manner to the the horizontal wind and temperature fields as follows

$$\frac{u^{t+k\Delta t_s} - u^{t'}}{\Delta t_s} = K_s \left(\frac{\partial^2 u}{\partial x^2} + \frac{\partial^2 u}{\partial y^2} \right)^{t'} + K_\sigma \left(\frac{\partial^2 u}{\partial \sigma^2} \right)^{,t'} \tag{4.77}$$

$$\frac{v^{t+k\Delta t_s} - v^{t'}}{\Delta t_s} = K_s \left(\frac{\partial^2 v}{\partial x^2} + \frac{\partial^2 v}{\partial y^2} \right)^{t'} + K_\sigma \left(\frac{\partial^2 v}{\partial \sigma^2} \right)^{t'}, \tag{4.78}$$

$$\frac{T^{t+k\Delta t_s} - T^{t'}}{\Delta t_s} = K_{Ts} \left(\frac{\partial^2 T}{\partial x^2} + \frac{\partial^2 T}{\partial y^2} \right)^{t'} + K_{T\sigma} \left(\frac{\partial^2 T}{\partial \sigma^2} \right)^{t'}. \tag{4.79}$$

Note that latest available values of the variables u, v, and T, as obtained after application of the adjustment procedure and the Shapiro filter, are used as initial values (denoted by time-level t') in (4.77) to (4.79). K_s and K_{Ts} are the horizontal diffusion coefficients, and K_σ and $K_{T\sigma}$ are the vertical diffusion coefficients. Typical values of the augmented diffusion coefficients $K\Delta t_s/\Delta n^2$ ($n = x$, y, σ) along the x, y and σ axis are respectively 0.0015, 0.0015 and 0.0015 for T and 0.015, 0.015 and 0.015 for u and v. Although the vertical momentum equation is not discretized explicitly, diffusion is applied to the vertical motion

field $\dot{\sigma}$ and p_s indirectly when the diffused horizontal motion field is used in the integration of (4.73) and (4.72).

Note that the dimensionless augmented diffusion coefficient $K\Delta t_s/\Delta n^2$ is convenient to use when the numerical values of the diffusion coefficients need to be specified. Janjic et al. (2001) used the same notation. The explicit diffusion step is the final phase of the split semi-Lagrangian scheme. After this step, all fields have been updated satisfactorily in order for the next semi-Lagrangian advection step to be performed.

4.6 Frequency response of the quasi-elastic equations to the forward-backward time discretization

In this section, the frequency response of the quasi-elastic equations to the forward-backward time discretization is examined using the von Neumann method (e.g. Richtmyer and Morton, 1967; Mesinger and Arakawa, 1976). As in the case of the linear analysis of the quasi-elastic equations performed in Chapter 3, the response analysis in the present section is carried out in two spatial dimensions.

In Chapter 3, the two-dimensional σ coordinate quasi-elastic equations (3.82)-(3.85) were linearized about an isothermal reference state of no motion, for a nonrotating, adiabatic and inviscid atmosphere. A similar linearization may be performed for the form that the two-dimensional equations assume in the adjustment step of the split semi-Lagrangian solution procedure. These linearized equations are:

$$\frac{\partial u}{\partial t} = -\left(\frac{\partial \phi^{'}}{\partial x}\right), \tag{4.80}$$

$$\frac{\partial p_s}{\partial t} = -p_0 \int_0^1 \frac{\partial u}{\partial x} d\sigma, \tag{4.81}$$

$$\dot{\sigma} = -\int_0^\sigma \left(\frac{\partial u}{\partial x}\right) d\sigma - \frac{\sigma}{p_0}\frac{\partial p_s}{\partial t}, \tag{4.82}$$

$$\frac{\partial T^{'}}{\partial t} = \kappa \left(\frac{p_0}{\sigma p_0 + p_T}\right)\left[\frac{\sigma}{p_0}\frac{\partial p_s}{\partial t} + \dot{\sigma}\right] T_0. \tag{4.83}$$

Equations (4.80) to (4.83) correspond to the linearized equations (3.102), (3.104) and (3.105), with the difference that the continuity equation is used in integrated form. That is, (4.81) and (4.82) replace (3.104) in order to obtain the linearized adjustment step equtions (before the time discretization is perfomed). Note once more that the vertical momentum equation is not used explicitly in the split semi-Lagrangian solution procedure. Following the procedure outlined

in Appendix A for the three-dimensional quasi-elastic σ coordinate equations, (3.102)-(3.105) can be shown to imply the linearized elliptic equation:

$$\frac{\partial^2 \phi^{'}}{\partial x^2} + \frac{\partial}{\partial \sigma}\left(s_0^2 \frac{\partial \phi^{'}}{\partial \sigma}\right) + \frac{\partial}{\partial \sigma}\left(s_0 \frac{T^{'}}{T_0} g\right) = 0. \tag{4.84}$$

Here $s_o = (1/H_0)\left(\sigma p_0 + p_T\right)/p_0 = (g/RT_0)\left(\sigma p_0 + p_T\right)/p_0$. Equation (4.84) is the linearized version of the elliptic equation (3.86), which is used in the split semi-Lagrangian discretization of the two-dimensional σ coordinate quasi-elastic equations.

Applying the forward-backward procedure presented in section 4.5 to solve the linearized equations (4.80) to (4.84) results in the following set of difference-differencial equations:

$$\frac{u^t - u^{t-\Delta t}}{\Delta t} = -\frac{\partial \phi^{'t-\Delta t}}{\partial x}, \tag{4.85}$$

$$\frac{p_s^t - p_s^{t-\Delta t}}{\Delta t} = -p_0 \int_0^1 \frac{\partial u^t}{\partial x} d\sigma, \tag{4.86}$$

$$\dot{\sigma}^t = -\int_0^\sigma \left(\frac{\partial u}{\partial x}\right)^t d\sigma - \frac{\sigma}{p_0}\frac{p_s^t - p_s^{t-\Delta t}}{\Delta t}, \tag{4.87}$$

$$\frac{T^{'t} - T^{'t-\Delta t}}{\Delta t} = \kappa\left(\frac{p_0}{\sigma p_0 + p_T}\right)\left[\frac{\sigma}{p_0}\left(\frac{p_s^t - p_s^{t-\Delta t}}{\Delta t}\right) + \dot{\sigma}^t\right] T_0, \tag{4.88}$$

$$\frac{\partial^2 \phi^{'t}}{\partial x^2} + \frac{\partial}{\partial \sigma}\left(s_0^2 \frac{\partial \phi^{'t}}{\partial \sigma}\right) = -\frac{\partial}{\partial \sigma}\left(s_0 \frac{T^{'t}}{T_0} g\right). \tag{4.89}$$

Note that, for the sake of convenience, the time-level notation is slightly different from that used for the advection step in section 4.5. Introducing Fourier decomposition of the form

$$\hat{Q}(\sigma)\exp^{i(kx - \vartheta t)} \tag{4.90}$$

for each variable, a response analysis of the time-discretized equations can be carried out for the corresponding amplitude functions. Note that $\vartheta = kc$ is the Eulerian frequency of the waves. By substituting (4.90) into (4.85)-(4.89) it is obtained that

$$\frac{\hat{u}}{\Delta t}\left(\exp^{-i\vartheta \Delta t} - 1\right) = -ik\hat{\phi^{'}}, \tag{4.91}$$

$$\frac{\hat{\pi}}{\Delta t}\left(1 - \exp^{i\vartheta \Delta t}\right) + ik\int_0^1 \hat{u}\, d\sigma = 0, \tag{4.92}$$

$$\hat{\dot{\sigma}} = -ik\int_0^{\sigma} \hat{u'}\, d\sigma - \frac{\sigma\hat{\pi}}{\Delta t}\left(1-\exp^{i\vartheta\Delta t}\right), \tag{4.93}$$

$$\frac{\hat{T'}}{\Delta t}\left(1-\exp^{i\vartheta\Delta t}\right) = \kappa\left(\frac{p_0}{\sigma p_0 + p_T}\right)\left[\frac{\sigma\hat{\pi}}{\Delta t}\left(1-\exp^{i\vartheta\Delta t}\right) + \hat{\dot{\sigma}}\right]T_0, \tag{4.94}$$

$$\frac{d}{d\sigma}\left[\left(\frac{\sigma p_0 + p_T}{p_0}\right)^2 \frac{d\hat{\phi'}}{d\sigma}\right] - H_0^2 k^2 \hat{\phi'} + H_0^2 \frac{d}{d\sigma}\left(s_0\hat{T}\frac{g}{T_0}\right) = 0. \tag{4.95}$$

Equation (4.95) may be written in terms of $\hat{\phi'}$ by using (4.91), (4.93) and (4.94). To this end, note that (4.94) may be used to show that

$$\frac{d}{d\sigma}\left(s_0\hat{T'}\right) = \frac{\Delta t\kappa}{H_0}\left[\frac{\hat{\pi}}{\Delta t}\left(1-\exp^{i\vartheta\Delta t}\right) + \frac{d\hat{\dot{\sigma}}}{d\sigma}\right]T_0\left(1-\exp^{i\vartheta\Delta t}\right)^{-1}. \tag{4.96}$$

Noting from (4.93) that

$$\frac{d\hat{\dot{\sigma}}}{d\sigma} = -ik\frac{d}{d\sigma}\int_0^{\sigma}\hat{u}\, d\sigma - \frac{\hat{\pi}}{\Delta t}\left(1-\exp^{i\vartheta\Delta t}\right), \tag{4.97}$$

it follows from substituting (4.97) in (4.96) and applying (4.91) that

$$\frac{d}{d\sigma}\left(s_0\hat{T'}\right) = -\frac{\kappa T_0}{H_0}\left[\frac{k^2\Delta t^2}{\left(\exp^{-i\vartheta\Delta t}-1\right)\left(1-\exp^{i\vartheta\Delta t}\right)}\right]\frac{d}{d\sigma}\int_0^{\sigma}\hat{\phi'}\, d\sigma \tag{4.98}$$

Substituting (4.98) in (4.95) leads to

$$\frac{d}{d\sigma}\left[\left(\frac{\sigma p_0 + p_T}{p_0}\right)^2 \frac{d\hat{\phi'}}{d\sigma}\right] - H_0^2 k^2 \hat{\phi'}$$

$$-H_0^2 N^2\left[\frac{k^2\Delta t^2}{\left(\exp^{-i\vartheta\Delta t}-1\right)\left(1-\exp^{i\vartheta\Delta t}\right)}\right]\frac{d}{d\sigma}\int_0^{\sigma}\hat{\phi'}\, d\sigma = 0. \tag{4.99}$$

Equation (4.99) is the vertical structure equation for $\hat{\phi'}$ that results from the forward-backward time discretization. Being of the same form as (3.113), the vertical structure equation of the undiscretized quasi-elastic equations, (4.99) admits solutions of the form (3.143). The corresponding dispersion relation obtained for the gravity waves is

$$m^2 = -\frac{1}{4H_0^2} + \left(\frac{N^2}{c_N^2} - k^2\right) > 0, \tag{4.100}$$

where $m > 0$ by definition and

$$c_N^2 = -\frac{\left(\exp^{-i\vartheta\Delta t} - 1\right)\left(1 - \exp^{i\vartheta\Delta t}\right)}{k^2\Delta t^2} = \frac{2\left(1 - \cos\vartheta\Delta t\right)}{k^2\Delta t^2}. \tag{4.101}$$

Equation (4.100) may be written in the alternative form

$$-k^2c_N^2\left(m^2 + k^2 + 1/4H_0^2\right)c^2 + k^2c^2N^2 = 0. \tag{4.102}$$

The form of (4.102) is identical to (3.142), the dispersion relation for the true frequency ϑ_T, with the substitution

$$\vartheta_T^2 = k^2c_N^2 = \frac{2\left(1 - \cos\vartheta\Delta t\right)}{\Delta t^2}. \tag{4.103}$$

Alternatively, the numerical value of the local frequency ϑ can be compared to its analytic counterpart ϑ_T through the relation

$$\vartheta = \frac{\arccos\left[1 - \left(\vartheta_T\Delta t\right)^2/2\right]}{\Delta t} \tag{4.104}$$

Clearly, (4.104) is defined for

$$-1 \leq 1 - \frac{\left(\vartheta_T\Delta t\right)^2}{2} < 1, \tag{4.105}$$

which may be written as

$$0 < \left|\vartheta_T\right|\Delta t \leq 2, \tag{4.106}$$

or alternatively as

$$0 < \frac{|c|\,\Delta t}{\Delta x} \leq \frac{2}{\pi}. \tag{4.107}$$

Here c denotes the analytic phase speed of the gravity waves. The relative frequency of the gravity waves in the numerical solution is defined as the ratio of the numerical frequency ϑ to the true frequency ϑ_T. That is,

$$R = \frac{\vartheta}{\vartheta_T} = \frac{\arccos\left[1 - \left(\vartheta_T\Delta t\right)^2/2\right]}{\Delta t\vartheta_T}, \tag{4.108}$$

provided that (4.106) is true. Recall the defenition of the Courant number, $\alpha = c\Delta t/\Delta x$. Equation (4.108) may alternatively be written in terms of α as

$$R = \frac{\vartheta}{\vartheta_T} = \frac{\arccos\left[1 - \left(k\Delta x\alpha\right)^2/2\right]}{k\Delta x\alpha}, \tag{4.109}$$

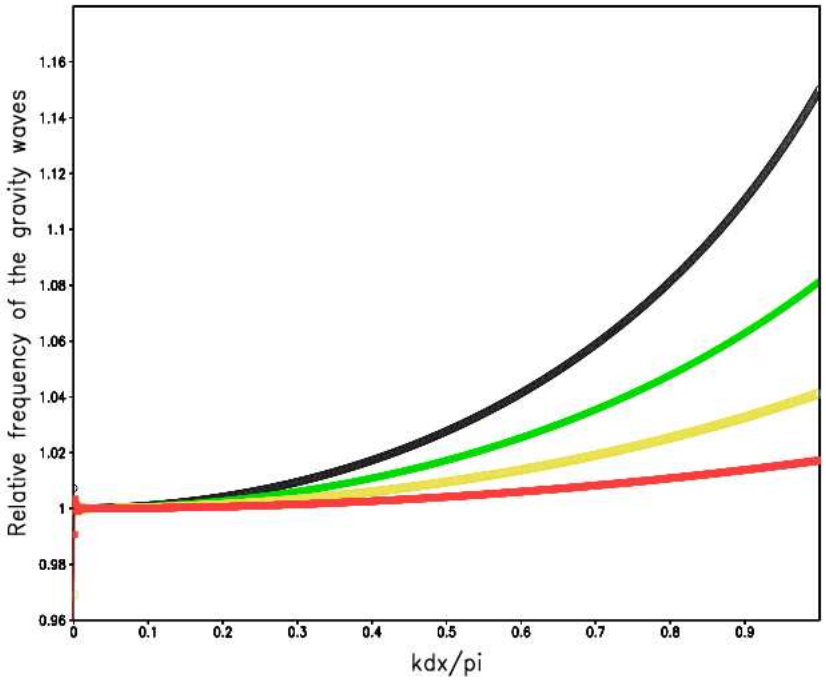

Figure 4.5: Relative frequency of the gravity waves in response to the forward-backward time discretization, as a function of the wave number. The red, yellow, green and black lines represent Courant numbers of 0.2, 0.3, 0.4 and 0.5, respectively.

noting the range of validity (4.107). The relative frequency of the gravity waves in the numerical solution is displayed in Fig. 4.5 for various values of α, as a function of the scaled wave number.

Condition (4.107) suggests that the forward-backward scheme can only be applied for Courant numbers less than or equal to $2/\pi$, else the numerical solution may have unphysical properties. This implies a significant restriction on the maximum size of the time-step that may be used during the adjustment step. From Fig. 4.5 it is evident that the forward-backward scheme accelerates the gravity waves. This artificial acceleration decreases as the wave length decreases, and in the long wave limit the numerical frequency (and phase speed) approaches the true frequency of the gravity waves. The acceleration also increases as the Courant number increases, by as much as 15% for $\alpha = 0.5$ at the shortest resolvable scales.

In practical applications of the split semi-Lagrangian scheme, the accelerating effect of the forward-backward scheme is alleviated by two factors: the damping effect of the bicubic spatial interpolations, particularly at short wave lengths (see section 4.2), and the explicit smoothing of the two-grid-interval wave by the Shapiro time filter (see section 4.4). The impact of these effects on the maximum size of time step that can be used in practical applications of the split semi-Lagrangian procedure, is investigated in Chapter 5 by means of numerical experiments.

4.7 Frequency response to spatial discretization on the nonstaggered grid

In this section, the frequency response to spatial discretization on the nonstaggered grid is examined, again using the von Neumann method (e.g. Rightmyer and Morton, 1967; Mesinger and Arakawa, 1976). As in the previous section, the two-dimensional quasi-elastic equations of the form used in the adjustment step are linearized about an isothermal reference state of no motion, for a non-rotating, adiabatic and inviscid atmosphere. The effect of numerical integration in the vertical (as applied to the continuity equation in order to evaluate p_s and $\dot{\sigma}$, see (4.81) and (4.82)) is not considered here, and in the frequency response analysis that follows, all vertical integrals are evaluated analytically.

4.7.1 Frequency response to horizontal discretization

When the horizontal spatial derivatives in (4.80) to (4.83) are discretized using second-order spatial differencing, and Fourier decomposition of the form (4.90) is performed on the resulting equations, the following amplitude equations result:

$$-i\vartheta\hat{u} = -i\left(\frac{\sin k\Delta x}{\Delta x}\right)\hat{\phi}, \tag{4.110}$$

$$-i\vartheta\hat{\pi} = -i\frac{\sin k\Delta x}{\Delta x}\int_0^1 \hat{u}\, d\sigma, \tag{4.111}$$

$$\hat{\dot{\sigma}} = -i\frac{\sin k\Delta x}{\Delta x}\int_0^\sigma \hat{u}\, d\sigma + i\vartheta\sigma\hat{\pi}, \tag{4.112}$$

$$-i\vartheta\hat{T}' = \kappa\left(\frac{p_0}{\sigma p_0 + p_T}\right)\left[-i\vartheta\sigma\hat{\pi} + \hat{\dot{\sigma}}\right]T_0. \tag{4.113}$$

The second horizontal derivative in (4.84) is left undiscretized, so that (4.95) is obtained after Fourier decomposition. Equation (4.95) is written in the form

$$\frac{d}{d\sigma}\left[\left(\frac{\sigma p_0 + p_T}{p_0}\right)^2\frac{d\hat{\phi}'}{d\sigma}\right] - H_0^2k^2\hat{\phi}' = -H_0^2\frac{d}{d\sigma}\left(s_0\hat{T}'\frac{g}{T_0}\right). \tag{4.114}$$

If the left-hand side of (4.114) is modified to include the effect of horizontal discretization, the frequency equation that results in combination with (4.110) to (4.113) can not be conveniently compared to its analytic counterpart (3.140). Thus, only the effect of horizontal discretization on the right-hand side of (4.114) (the forcing to which the geopotential distribution respond to) will be considered.

The right-hand side of (4.114) can be written in terms of $\hat{\phi}'$ by using (4.110) to (4.113). To this end, note that by using (4.113) it may be shown that

$$\frac{d}{d\sigma}\left(s_0\hat{T}'\right) = \frac{\kappa}{H_0}\left(\hat{\pi} - \frac{1}{i\vartheta}\frac{d\hat{\dot{\sigma}}}{d\sigma}\right)T_0. \tag{4.115}$$

Noting from (4.112) that

$$\frac{d\hat{\dot{\sigma}}}{d\sigma} = -i\frac{\sin k\Delta x}{\Delta x}\frac{d}{d\sigma}\left(\int_0^\sigma \hat{u}d\sigma\right) + i\vartheta\hat{\pi}, \tag{4.116}$$

it follows by applying (4.116) and making use of (4.110) that

$$\frac{d}{d\sigma}\left(s_0\hat{T}\right) = \frac{\kappa}{H_0}\left(\frac{1}{\vartheta^2}\frac{\sin^2 k\Delta x}{\Delta x^2}\right)\left(\frac{d}{d\sigma}\int_0^\sigma \hat{\phi}'\, d\sigma\right)T_0. \tag{4.117}$$

Substituting (4.117) in (4.114) leads to a vertical structure equation for $\hat{\phi}'$,

$$\frac{d}{d\sigma}\left[\left(\frac{\sigma p_0 + p_T}{p_0}\right)^2\frac{d\hat{\phi}'}{d\sigma}\right] - H_0^2k^2\hat{\phi}' + \frac{H_0^2N^2}{\vartheta^2}\left(\frac{\sin^2 k\Delta x}{\Delta x^2}\right)\frac{d}{d\sigma}\int_0^\sigma \hat{\phi}'\, d\sigma = 0. \tag{4.118}$$

Equation (4.118) is of the same form as (3.113), the vertical structure equation for the undiscretized quasi-elastic equations. It therefore admits solutions of the form (3.143). Substituting (3.143) in (4.118) leads to the frequency equation

$$\mu^2 = \frac{1}{4H_0^2} - \left(\frac{N^2}{\vartheta^2} \frac{\sin^2 k\Delta x}{\Delta x^2} - k^2 \right). \tag{4.119}$$

The form of (4.119) is identical to (3.118), the analytic dispersion for the true frequency ϑ_T, with the substitution

$$\frac{1}{\vartheta_T^2} = \frac{1}{\vartheta^2} \frac{\sin^2 k\Delta x}{k^2 \Delta x^2}. \tag{4.120}$$

That is, the numerical value of the local frequency may be compared to its analytic counterpart ϑ_T through the relation

$$\vartheta^2 = \vartheta_T^2 \frac{\sin^2 k\Delta x}{k^2 \Delta x^2}. \tag{4.121}$$

The relative frequency of oscillations in the numerical model using second order spatial differencing may therefore be defined as

$$R_2 = \frac{\vartheta}{\vartheta_T} = \frac{\sin k\Delta x}{k\Delta x}. \tag{4.122}$$

Through a similar derivation process, one may show that the relative frequencies of oscillations in the numerical model for fourth and sixth-order differencing are respectively

$$R_4 = \frac{1}{k\Delta x} \left(\frac{4}{3} \sin k\Delta x - \frac{1}{6} \sin 2k\Delta x \right), \tag{4.123}$$

$$R_6 = \frac{1}{k\Delta x} \left(\frac{3}{2} \sin k\Delta x - \frac{3}{10} \sin 2k\Delta x + \frac{1}{30} \sin 3k\Delta x \right). \tag{4.124}$$

The relative frequencies (4.122) to (4.124) correspond exactly to (4.47), (4.53) and (4.59), the corresponding relative frequency equations for centered differencing as applied to the pure gravity waves on the nonstaggered grid. Fig. 4.3 and the discussion in section 4.3 therefore also apply to the quasi-elastic equations when discretized with centered differences on the nonstaggered grid.

4.7.2 Frequency response to vertical discretization

In order to investigate the frequency response of the quasi-elastic equations on the nonstaggered grid, it may first be noted that the linearized adjustment step equations (4.80) to (4.83) contain no vertical derivatives. Performing Fourier decomposition of the form (4.90) on (4.80) to (4.83) gives the amplitude equations

$$-i\vartheta\hat{u} = -ik\hat{\phi}, \tag{4.125}$$

$$-i\vartheta\hat{\pi} = -ik\int_0^1 \hat{u}\,d\sigma, \tag{4.126}$$

$$\hat{\dot{\sigma}} = -ik\int_0^\sigma \hat{u}\,d\sigma + i\vartheta\sigma\hat{\pi}, \tag{4.127}$$

$$-i\vartheta\hat{T}' = \kappa\left(\frac{p_0}{\sigma p_0 + p_T}\right)\left[-i\vartheta\sigma\hat{\pi} + \hat{\dot{\sigma}}\right]T_0. \tag{4.128}$$

Note once more that the integrals over σ in (4.126) and (4.127) will be treated analytically in the following analysis. By substituting (4.127) in (4.128), and by applying (4.125), the following equation for $\hat{T}'$ in terms of $\hat{\phi}'$ may be obtained:

$$\hat{T}' = \frac{k^2}{\vartheta^2}\kappa T_0\left(\frac{p_0}{\sigma p_0 + p_T}\right)\int_0^\sigma \hat{\phi}'\,d\sigma. \tag{4.129}$$

Substituting (4.129) into the linearized elliptic equation (4.95), gives the following vertical structure equation for $\hat{\phi}'$:

$$\frac{\partial^2\phi'}{\partial x^2} + \frac{\partial}{\partial\sigma}\left(s_0^2\frac{\partial\phi'}{\partial\sigma}\right) = -H_0^2\frac{N^2k^2}{\vartheta^2}\frac{d}{d\sigma}\int_0^\sigma \hat{\phi}'\,d\sigma. \tag{4.130}$$

In order to perform the frequency response analysis to vertical discretization on the nonstaggered grid, (4.130) is written in terms of Z using transformation relationships (3.114) and (C.1). The resulting equation is

$$H_0^2\frac{d^2\hat{\phi}'}{dZ^2} - H_0\frac{d\hat{\phi}'}{dZ} - k^2H_0^2\hat{\phi}' = \underbrace{-H_0^2\frac{N^2k^2}{\vartheta^2}\exp^{Z/H_0}\frac{d}{dZ}\int_{Z|_{\sigma=0}}^{Z|_\sigma}\hat{\phi}'\exp^{-Z/H_0}\,dZ}_{X}\,. \tag{4.131}$$

Equation (4.131) is the vertical structure equation for $\hat{\phi}'$ in terms of Z, it admits solutions of the form

$$\hat{\phi}' = \exp^{(im+1/2H_0)Z} \tag{4.132}$$

(see Chapter 3). The vertical derivatives in (4.131) may now be discretized and wave-like solutions of the form (4.132) substituted in the resulting equation. However, the dispersion relationship that results can not be compared directly to the analytic relationship (3.140) that applies to the undiscretized quasi-elastic equations. A more useful expression is obtained when only the right-hand side of equation (4.131), term X, is discretized. This term represents the main forcing effect to which the geopotential distribution respond.

4.7.2.1 Second order vertical differencing

Substituting wave like solutions of the form (4.132) in (4.131), and using second order differencing to approximate the vertical derivative in term X, gives the dispersion relationship

$$m^2 = -\frac{1}{4H_0^2} + \left[\frac{N^2k^2}{\vartheta^2}\left(\frac{1}{im - 1/2H_0}\right)D_{A2} - k^2\right], \tag{4.133}$$

where

$$D_{A2} = \frac{\exp^{(im-1/2H_0)\Delta Z} - \exp^{-(im-1/2H_0)\Delta Z}}{2\Delta Z}. \tag{4.134}$$

The form of (4.133) is identical to that of the analytic dispersion for the true frequency ϑ_T of the quasi-elastic equations, with the substitution:

$$\frac{1}{\vartheta_T^2} = \frac{1}{\vartheta^2}\left(\frac{1}{im - 1/2H_0}\right)D_{A2}. \tag{4.135}$$

The frequencies of gravity wave oscillations in the numerical model are therefore related to the analytical ones via the relation

$$\vartheta^2 = \vartheta_T^2\left(\frac{1}{im - 1/2H_0}\right)D_{A2}. \tag{4.136}$$

The magnitude of the relative frequency of oscillations in the numerical model using second order spatial differencing may therefore be defined as

$$R_{A2} = \left|\frac{\vartheta}{\vartheta_T}\right| = \left|\left(\frac{D_{A2}}{im - 1/2H_0}\right)^{1/2}\right|. \tag{4.137}$$

Note that D_{A2} may be written as

$$D_{A2} = \frac{\cos m\Delta Z\left(\exp^{-\Delta Z/2H_0} - \exp^{\Delta Z/2H_0}\right)}{2\Delta Z} +$$

$$\frac{i\sin m\Delta Z\left(\exp^{-\Delta Z/2H_0} + \exp^{\Delta Z/2H_0}\right)}{2\Delta Z}. \tag{4.138}$$

The magnitude of the relative frequency R_{A2} for second order differencing is displayed in Fig. 4.6 for $\Delta Z = 100\,m$ and $0 < m\Delta Z/\pi \leq 1$ (black line). It may be noted that the retardation of wave frequencies due to discretization on the nontstaggered grid is the highest for large wave numbers (shorter wave lengths). The $2\Delta Z$ wave is almost stationary. In the long wave limit, the numerical frequency of waves approaches the analytical frequency.

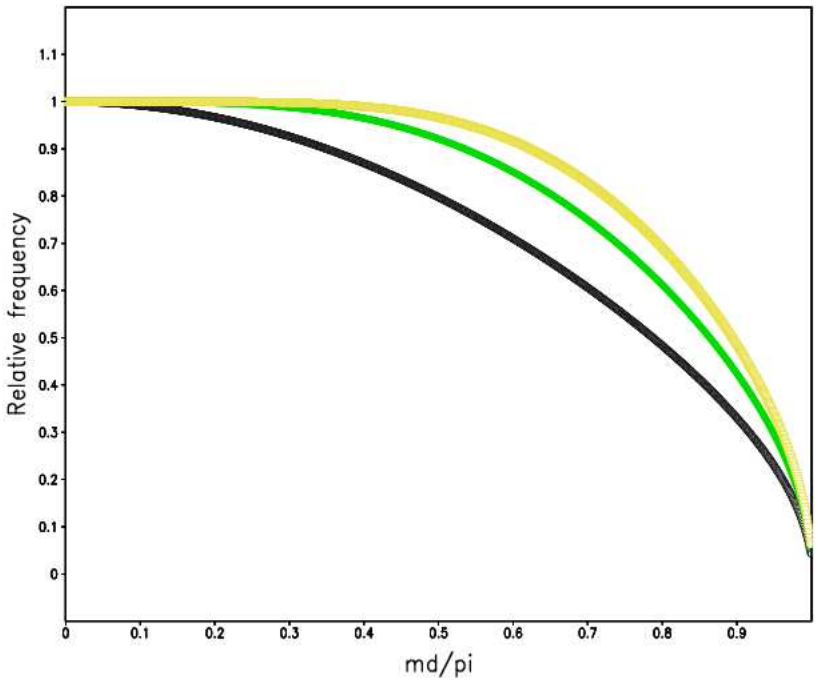

Figure 4.6: Relative frequency of the gravity waves described by the quasi-elastic equations, in response to centered finite diferencing in the vertical on the nonstaggered grid, as a function of the vertical wave number. The black, green and yellow lines represent second, fourth and sixth order differencing, respectively.

4.7.2.2 Fourth order vertical differencing

When fourth order differencing is used to approximate the vertical derivative in term X of (4.131), the resulting dispersion relationship is:

$$m^2 = -\frac{1}{4H_0^2} + \left[\frac{N^2k^2}{\Omega^2}\left(\frac{1}{im - 1/2H_0}\right) D_{A4} - k^2\right], \tag{4.139}$$

where

$$D_{A4} = \frac{1}{12}\left[\frac{\exp^{-(im-1/2H_0)2\Delta Z} - \exp^{(im-1/2H_0)2\Delta Z}}{\Delta Z}\right] +$$

$$\frac{2}{3}\left[\frac{\exp^{(im-1/2H_0)\Delta Z} - \exp^{-(im-1/2H_0)\Delta Z}}{\Delta Z}\right]. \tag{4.140}$$

The form of (4.139) is identical to that of the analytic dispersion (3.140) for the true frequency ϑ_T of the quasi-elastic equations, with the substitution:

$$\frac{1}{\vartheta_T^2} = \frac{1}{\vartheta^2}\left(\frac{1}{im - 1/2H_0}\right) D_{A4}. \tag{4.141}$$

The frequencies of gravity wave oscillations in the numerical model with fourth order spatial differencing are therefore related to the analytical ones via the relation

$$\vartheta^2 = \vartheta_T^2\left(\frac{1}{im - 1/2H_0}\right) D_{A4}. \tag{4.142}$$

The magnitude of the relative frequency of oscillations in the numerical model using fourth order spatial differencing may therefore be defined as

$$R_{A4} = \left|\frac{\vartheta}{\vartheta_T}\right| = \left|\left(\frac{D_{A4}}{im - 1/2H_0}\right)^{1/2}\right|. \tag{4.143}$$

Note that D_{A4} may be written as

$$D_{A4} = \frac{1}{12\Delta Z}\cos 2m\Delta Z\left(\exp^{\Delta Z/H_0} - \exp^{-\Delta Z/H_0}\right) +$$

$$\frac{2}{3\Delta Z}\cos m\Delta Z\left(\exp^{-\Delta Z/2H_0} - \exp^{\Delta Z/2H_0}\right) +$$

$$i\frac{1}{12\Delta Z}\sin 2m\Delta Z\left(-\exp^{\Delta Z/H_0} - \exp^{-\Delta Z/H_0}\right) +$$

$$i\frac{2}{3\Delta Z}\sin m\Delta Z\left(\exp^{-\Delta Z/2H_0} + \exp^{-\Delta Z/2H_0}\right). \tag{4.144}$$

The magnitude of the relative frequency R_{A4} for fourth order differencing is displayed in Fig. 4.4 for $\Delta Z = 100\,m$ and $0 < m\Delta Z/\pi \leq 1$ (green line). The improvement gained from fourth order differencing compared to second order differncing is the largest (about 10-20%) for short waves lengths (note that a normalized wave numer of 0.5 corresponds to the $4\Delta Z$ wave). The $2\Delta Z$ waves remain significantly retarded, howevever.

4.7.2.3 Sixth order vertical differencing

Using sixth order differencing to approximate the vertical derivative in term X of equation (4.131), the resulting dispersion relationship is:

$$m^2 = -\frac{1}{4H_0^2} + \left[\frac{N^2k^2}{\vartheta^2}\left(\frac{1}{im - 1/2H_0}\right) D_{A6} - k^2\right], \tag{4.145}$$

where

$$D_{A6} = \frac{1}{60}\left[\frac{\exp^{(im-1/2H_0)3\Delta Z} - \exp^{-(im-1/2H_0)3\Delta Z}}{\Delta Z}\right] +$$

$$\frac{3}{20}\left[\frac{\exp^{-(im-1/2H_0)2\Delta Z} - \exp^{(im-1/2H_0)2\Delta Z}}{\Delta Z}\right] +$$

$$\frac{3}{4}\left[\frac{\exp^{(im-1/2H_0)\Delta Z} - \exp^{-(im-1/2H_0)\Delta Z}}{\Delta Z}\right]. \tag{4.146}$$

The form of (4.145) is identical to that of the analytic dispersion (3.140) for the true frequency ϑ_T of the quasi-elastic equations, with the substitution:

$$\frac{1}{\vartheta_T^2} = \frac{1}{\vartheta^2}\left(\frac{1}{im - 1/2H_0}\right) D_{A6}. \tag{4.147}$$

The frequencies of gravity wave oscillations in the numerical model with sixth order spatial differencing are therefore related to the analytical ones via the relation

$$\vartheta^2 = \vartheta_T^2\left(\frac{1}{im - 1/2H_0}\right) D_{A6}. \tag{4.148}$$

The magnitude of the relative frequency of oscillations in the numerical model using sixth order spatial differencing may therefore be defined as

$$R_{A6} = \left|\frac{\vartheta}{\vartheta_T}\right| = \left|\left(\frac{D_{A4}}{im - 1/2H_0}\right)^{1/2}\right|. \tag{4.149}$$

Note that D_{A6} may be written as

$$D_{A6} = \frac{1}{60\Delta Z}\cos 3m\Delta Z\left(\exp^{-3\Delta Z/2H_0} - \exp^{3\Delta Z/2H_0}\right) +$$

$$\frac{3}{20\Delta Z}\cos 2m\Delta Z\left(\exp^{\Delta Z/H_0} - \exp^{-\Delta Z/H_0}\right) +$$

$$\frac{3}{4\Delta Z}\cos m\Delta Z\left(\exp^{-\Delta Z/2H_0} - \exp^{\Delta Z/2H_0}\right) +$$

$$i\frac{1}{60\Delta Z}\sin 3m\Delta Z\left(\exp^{-3\Delta Z/2H_0} + \exp^{3\Delta Z/2H_0}\right) +$$

$$i\frac{3}{20\Delta Z}\sin 2m\Delta Z\left(-\exp^{\Delta Z/H_0} - \exp^{-\Delta Z/H_0}\right) +$$

$$i\frac{3}{4\Delta Z}\sin m\Delta Z\left(\exp^{-\Delta Z/2H_0} + \exp^{\Delta Z/2H_0}\right). \qquad (4.150)$$

The magnitude of the relative frequency R_{A6} for sixth order differencing is displayed in Fig. 4.6 for $\Delta Z = 100\,m$ and $0 < m\Delta Z/\pi \leq 1$ (yellow line). Sixth order differencing results in an improvement of 15-25% in the representation of the frequency of short waves, compared to second order differencing. The $2\Delta Z$ wave remains significantly retarded.

More insight into the advantages of higher order differencing on the nonstaggered grid may be gained by considering Fig. 4.7. Here the relative frequencies corresponding to second (black), fourth (green line) and sixth (yellow line) order differencing are shown as a function of wavelength. $\Delta Z = 100\,m$, so that the shortest resolvable waves at this resolution have wave length $200\,m$. The red line in the figure represents the relative frequency obtained from using second order differencing with $\Delta Z = 50\,m$. It can be seen that from Fig. 4.7 that both fourth and sixth order differencing provide a significant improvement over second order differencing, particularly at short wave lengths. In fact, fourth and sixth order differencing provide more accurate results than second order differencing performed at double the resolution, for wave lengths longer than four grid lengths and three grid lengths respectively. At the shortest resolvable scales, the gravity waves are significantly retarded, for all the differencing schemes. However, it is useful to note that the two-grid-interval waves are not completely stationary as in the case of horizontal spatial differencing. Note that near the vertical boundaries of a numerical model the application of sixth or even fourth order differencing may be either impractical, or may require that artificial boundary conditions are specified.

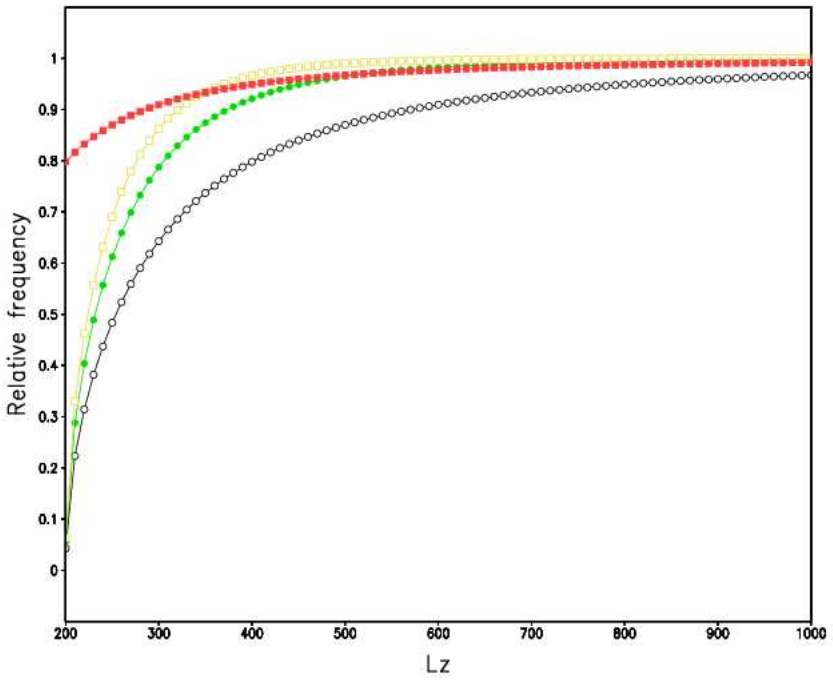

Figure 4.7: Relative frequency of the gravity waves described by the quasi-elastic equations, in response to centered finite diferencing in the vertical on the nonstaggered grid, as a function of the vertical wave length. The black, green and yellow lines represent second, fourth and sixth order differencing, respectively, with $\Delta Z = 100\,m$. The red line was obtained using second order differencing with $\Delta Z = 50\,m$.

4.8 Elliptic solvers for the diagnostic equation in the geopotential

As a final step in the adjustment procedure, the elliptic equations (3.81) and (3.86) need to be solved for three and two-dimensional applications respectively. Closely related elliptic equations are solved in the σ coordinate version of the MP equations (e.g. Xue, 1989; Xue and Thorpe, 1991) and in the anelastic σ coordinate NHAD model (Room et al., 2000). An efficient solution procedure to solve the elliptic eqution in the σ coordinate MP model was devised by Xue (1989). This method is based on the Fast Fourier Transform (FFT) technique. It involves the linerarization of certain terms in (3.81) and (3.86), and a careful consideration of the lower boundary conditions imposed on ϕ. Certain pre- and post-processing is necessary, in order to achieve maximum efficiency of the FFT subroutines (see Wilhelmson and Ericksen, 1976). A similar solution procedure was used by Room et al. (2001) to solve the elliptic equation implied by the anelastic σ coordinate equations. However, the FFT method of Xue (1989) is complicated and elaborate to code, and needs the implementation of some specific software. In the present study, where a completly new code for a new atmospheric model is developed, it was decided to rather develop an independently coded elliptic solver to solve equations (3.81) and (3.86). Successive Over-Relaxation (SOR) (see Burden and Faires, 1993), an iterative procedure, is used in the present study. This flexible technique is relatively easy to code and far more convenient to use during the development phase of a new model than the more complicated FFT techniques.

Unfortunately, the SOR method generally suffers from progressively slow convergence with the increase in model resolution, and the increase in the number of data points in the discretized elliptic operator (Xue, 1989). The efficiency of the SOR solution procedure developed in this section is discussed in Chapter 5, in the context of the numerical experiments performed in that Chapter. It is shown that the method is reasonably efficient for the tests performed, generally requiring only a few iterations per adjustment time step. Solving the elliptic equation represents a fundamental part of the computational costs of the model. It will be beneficial to implement a more efficient solution procedure, possibly based on the FFT method of Xue (1989), for the potential operational application of the model in the future. Still, it should be realized that the nature of the problem of solving the elliptic equation, namely that the solution at any point depends on all the conditions of the entire boundary, makes the numerical problem global. All the data points have to be in the core computer memory at the same instant. This will always make the solution of a three-dimensional elliptic equation expensive, even for the commercially available solvers based on transformation techniques or matrix inversion techniques based on tri-diagonalisation.

In what follows, the numerical discretization of the elliptic equation as used in the model will be discussed in two dimensions only, in order to keep the notation

simple. The extension of the solution procedure to three dimensons is obvious.

In section 4.6 equation (3.86) is linearized around an isothermal reference state of no motion to obtain (4.84). Equation (4.84) indicates that only the terms $\partial^2\phi/\partial x^2$and $\partial\left(s^2\partial\phi/\partial\sigma\right)/\partial\sigma$ are dominant in (3.86). The coefficients of the remaining terms on the left hand side of (3.86) are due to the variation of the surface pressure, and generally much smaller than those of the dominant terms (Xue, 1989). Following (Xue, 1989), the less important terms are moved to the right hand side and treated explicitly, in order to obtain a nearly standard Poison equation:

$$\left[\frac{\partial^2}{\partial x^2}+\frac{\partial}{\partial\sigma}\left(s^2\frac{\partial\phi}{\partial\sigma}\right)\right]\phi^{p+1}=L\left(\phi^p\right)+F_\phi. \tag{4.151}$$

Here 'p' denotes the p_{th} iteration,

$$L=-2\sigma\frac{\partial\ln p_s}{\partial x}\frac{\partial^2}{\partial x\partial\sigma}+\left(\frac{\partial\ln p_s}{\partial x}\right)^2\frac{\partial}{\partial\sigma}\left(\sigma^2\frac{\partial}{\partial\sigma}\right)-\frac{\sigma}{p_s}\left(\frac{\partial^2 p_s}{\partial x^2}\right)\frac{\partial}{\partial\sigma} \tag{4.152}$$

and

$$F_\phi=2\left[\frac{\partial u}{\partial x}\frac{\partial}{\partial\sigma}\left(\Omega\frac{p}{p_s}\right)-\frac{1}{p_s}\frac{\partial}{\partial x}\left(\Omega p\right)\frac{\partial u}{\partial\sigma}\right]-\frac{\partial}{\partial\sigma}\left[\left(sg\right)-\frac{1}{\gamma}\frac{p}{p_s}\Omega^2\right]. \tag{4.153}$$

Note that s in (4.153) is not linearized over x, as in the corresponding equation used by Xue (1989).

4.8.1 Spatial discretization

By discretizing the terms in (4.151) using the second order accurate differencing formulas (4.27) and (4.35), an iterative solution procedure of (4.151) based on SOR may be constructed (see Burden and Faires (1993) for a discussion of the SOR technique). This solution procedure will be referred to as the "second order solver" in the remainder of the text.

When the first derivatives in the adjustment step terms (section 4.5) are evaluated by using the fourth order spatial differencing operator (4.28), inconsistencies with the second order discretization of (4.151) leads to divergence of the SOR procedure (this was established while conducting the numerical experiments described in Chapter 5). Therefore, a "fourth order solver" was developed, where (4.151) is discretized using the fourth order accurate operators (4.28) and (4.36), and then solved iteratively using SOR. Because the spatial derivatives in the adjustment step and in the fourth order solver are evaluated consistently in this case, the SOR procedure in the fourth order solver was found to be convergent.

Similarly, a sixth-order discretization of the spatial derivatives in the adjustment step would be inconsistent with both the second and fourth order solvers, and divergence of the SOR procedure would occur. A sixth order solver needs to be constructed using the operatores (4.30) and (4.37), to obtain the convergence of iterations for the case of a sixth order discretization of the adjustment step terms. However, such a high-order solver is elaborate and cumbersome to code, and the SOR technique generally suffers from slower convergence if the number of data points in the discretized operator increases (Xue, 1989). Therefore, an elliptic solver beyond fourth order discretization was not constructed in this study.

4.8.2 Convergence of iterations

The criterion of convergence of iterations is

$$\frac{\sqrt{\Sigma_{i,j}\left(\phi^{p+1}-\phi^{p}\right)^{2}}}{\sqrt{\Sigma_{i,j}\left(\phi^{p+1}\right)^{2}}}<\epsilon$$

with $\epsilon = 10^{-6}$ being used in the model, except in the initialization step where $\epsilon = 10^{-6}/5$ is required for sufficient convergence of the solution. In the experiments described in Chapter 5, a relaxation coefficient $rl = 1.9$ (see Burden and Faires, 1993) was found to generally result in the fastest convergence. The efficiency of the elliptic solver and the convergence of iterations are discussed in more detail in Chapter 5.

4.9 Boundary conditions

In this section, lateral and vertical boundary conditions are formulated for the new model based on the split semi-Lagrange solution of the quasi-elastic equations. These boundary conditions are suitable for the series of numerical tests performed in Chapter 5. For more general, real-atmosphere applications of the model, the lateral boundary conditions in particular would need some modification (see the discussion in section 4.9.1). The boundary conditions are applied after each adjustment step in the solution procedure. The boundary conditions are stated for three-dimensional applications of the new model, the simplifications needed for two-dimensional applications are obvious.

4.9.1 Lateral boundary conditions

Unless stated otherwise for a specific experiment, the lateral boundary conditions used in the model in order to perform the numerical experiments described in Chapter 5 are:

$$\frac{\partial \ln p_s}{\partial x}=\frac{\partial \ln p_s}{\partial y}=0, \tag{4.154}$$

$$\frac{\partial T}{\partial x} = \frac{\partial T}{\partial y} = 0, \tag{4.155}$$

$$\frac{\partial \phi}{\partial x} = \frac{\partial \phi}{\partial y} = 0, \tag{4.156}$$

$$u = v = 0, \tag{4.157}$$

$$\frac{\partial \dot{\sigma}}{\partial x} = \frac{\partial \dot{\sigma}}{\partial y} = 0, \tag{4.158}$$

$$\frac{\partial \Omega}{\partial x} = \frac{\partial \Omega}{\partial y} = 0. \tag{4.159}$$

No-stress boundary conditions are imposed on the velocity field, which imply at the lateral boundaries that the horizontal derivatives of $\dot{\sigma}$ and the horizontal velocity field vanish (4.157 and 4.158). It is assumed that the horizontal derivatives of p_s, T and ϕ vanish at the lateral boundaries (4.154 to 4.156). From (4.154) and (4.158) it follows by the use of (3.69) that the horizontal derivatives of Ω will also vanish at the lateral boundaries (4.159).

At the lateral boundaries, the transformed surface pressure p_s and vertical velocity $\dot{\sigma}$ may alternatively be calculated from the continuity equation, similar to the approach followed by Xue and Thorpe (1991). The lateral boundary condition $u = v = 0$ is limiting in the sense that flow is not allowed through the lateral boundaries. For typical atmospheric flows in the westerly wind-regime, there is a zonal wind component that causes an inflow at the western boundary and an outflow at the eastern boundary. At the outflow boundary there is the possibility of developing numerical reflection, i.e. a numerical wave may unphysically interact with the boundary and energy in the numerical flow may travel backwards. An experiment with non-zero flow over the lateral boundaries is performed in section 5.6, however, the lateral boundaries are chosen to be far away from the flow features of interest in order to avoid potential boundary reflection problems. Careful consideration of the lateral boundary reflection problem will be required for real-atmosphere applications of the model. For such applications, lateral boundary conditions may be obtained from a forcing model that runs over a larger domain at lower resolution, that is, from a standard nesting procedure. An alternative suitable for some applications, would be to apply the radiative boundary condition (Orlanski, 1976) to the horizontal velocity field, the temperature T and transformed surface pressure p_s, following Xue and Thorpe (1991) and Miller and Thorpe (1981).

4.9.2 Lower and upper boundary conditions

The lower boundary of the model ($\sigma = 1$) is the ground surface. The model top ($\sigma = 0$) where $p = p_T = constant$ is a free surface, where external gravity waves are supported. The lower and upper boundary conditions for the various variables may be specified as follows:

4.9.2.1 Temperature field

At the top and bottom surfaces, a zero vertical gradient boundary condition is imposed on the potential temperature θ, that is, $\partial\theta/\partial\sigma = 0$. From this condition and the potential temperature definition

$$\theta = T\left(\frac{p_{STAN}}{p}\right)^{R/c_p}, \tag{4.160}$$

it follows that that in terms of the temperature field

$$T|_{\sigma=1} = T|_{\sigma=1-\Delta\sigma}\left[\frac{p_s + p_T}{(1-\Delta\sigma)\,p_s + p_T}\right]^{R/c_p} \tag{4.161}$$

and

$$T|_{\sigma=0} = T_{\sigma=\Delta\sigma}\left(\frac{p_T}{\Delta\sigma p_s + p_T}\right)^{R/c_p}, \tag{4.162}$$

for the lower and upper boundaries respectively. Note that p_s is the augmented surface pressure, whilst p_{STAN} denotes a standard reference pressure level. Equations (4.161) and (4.162) are applied as boundary conditions on the temperature field in the model.

It is worthwhile to note that, from the definition of potential temperature,

$$\frac{\partial\theta}{\partial\sigma} = 0 \Rightarrow \frac{\partial T}{\partial\sigma} = \frac{1}{c_p}\frac{p_s}{p}RT. \tag{4.163}$$

4.9.2.2 Geopotential field

The lower boundary condition imposed on ϕ is simply

$$\phi|_{\sigma=1} = h\,(x,\,y)\,g, \tag{4.164}$$

with $h(x, y)$ the actual terrain height and g is the gravitational acceleration defined earlier. Note that in the case of zero surface topography, condition (4.164) implies that $\phi|_{\sigma=1} = 0$.

Assuming hydrostatic balance and integrating over the top model layer gives:

$$\phi|_{\sigma=0} - \phi|_{\sigma=\Delta\sigma} = -R \int_{\sigma=\Delta\sigma}^{0} \frac{p_s}{p} T \, d\sigma \tag{4.165}$$

The assumption of hydrostatic balance over the top model layer is consistent with the linear analysis of the quasi-elastic equations discussed in Chapter 3. Integrating (4.163) over the top model layer, where $\partial\theta/\partial\sigma = 0$, gives:

$$T|_{\sigma=0} - T|_{\sigma=\Delta\sigma} = \frac{R}{c_p} \int_{\sigma=\Delta\sigma}^{0} \frac{p_s}{p} T \, d\sigma. \tag{4.166}$$

Combining (4.163) and (4.166) yields the upper boundary condition on ϕ that is used in the model:

$$\phi|_{\sigma=0} = \phi|_{\sigma=\Delta\sigma} - c_p \left(T|_{\sigma=0} - T|_{\sigma=\Delta\sigma} \right). \tag{4.167}$$

The vertical boundary conditions imposed on ϕ are much simpler than those used in σ coordinate numerical realizations of the MP and NHAD models, where the use of a reference geopotential profile induces a more complicated treatment (Xue and Thorpe, 1991; Room et al., 2001). The anelastic σ coordinate equations of Room et al. (2001) require additional careful treatment of the vertical boundary conditions imposed on ϕ, in order to ensure mass conservation in the model.

4.9.2.3 Velocity field

The no-stress boundary conditions imposed on the velocity field imply at the vertical boundaries ($\sigma = 1$ and $\sigma = 0$) that the vertical derivative of the horizontal wind is assumed to vanish. By definition, $\dot{\sigma} = 0$ at $\sigma = 1$ and $\sigma = 0$. In equation form, the vertical boundary conditions imposed on the velocity field are:

$$\dot{\sigma}|_{\sigma=1} = \dot{\sigma}|_{\sigma=0} = 0 \tag{4.168}$$

and

$$\frac{\partial u}{\partial \sigma}|_{\sigma=0} = \frac{\partial u}{\partial \sigma}|_{\sigma=1} = \frac{\partial v}{\partial \sigma}|_{\sigma=0} = \frac{\partial v}{\partial \sigma}|_{\sigma=1} = 0. \tag{4.169}$$

Vertical boundary conditions also need to be specified for variable $\Omega = \omega/p$. At the model top (a fixed pressure level),

$$\Omega|_{\sigma=0} = 0,$$

whilst the lower boundary condition on $\dot{\sigma}$ (4.168) implies that

$$\Omega|_{\sigma=1} = \left(\frac{p_s}{p_s + p_T} \frac{D \ln p_s}{Dt} \right),$$

by (3.69).

4.10 Comparison of the split semi-Lagrangian scheme to the numerics of the MP and NHAD models

It is useful to compare the properties of the split semi-Lagrangian procedure used to solve the quasi-elastic equations to those of the numerical methods used in the closely related σ coordinate MP and NHAD models:

- The split semi-Lagrangian scheme is formulated as a two time-level scheme, which implies that no computational modes are present, and there is no need for time-filtering. The explicit leap-frog scheme is applied in the σ coordinate numerical realizations of the MP and NHAD models (e.g. Xue and Thorpe, 1991; Miranda and James, 1992; Room et al., 2001). The leap-frog scheme is a three time-level scheme, and requires the use of a time filter in order to prevent decoupling of the numerical solution in time. The Robert-Asselin filtering technique (Robert, 1966; Asselin, 1972) is applied in the MP and NHAD models for this purpose (Xue and Thorpe, 1991; Miranda and James, 1992; Room et al., 2001).

- The MP and NHAD models employ a flux formulation of the relevant σ coordinate equations, whilst the advective formulation of the quasi-elastic equations is used for formulating the split semi-Lagrangian procedure.

- Eulerian procedures are used in the MP and NHAD models. This, in combination with the leapfrog-scheme for time integration, yields that the MP and NHAD models are stable under the CFL condition. This implies a restriction on the maximum size of time-step that may be used in these models. The split semi-Lagrangian procedure offers a computationally more efficient procedure. Courant numbers larger than unity (associated with relatively large time steps) may occur during the semi-Lagrangian advection step, without a compromise of numerical stability (see section 4.2 and Chapter 5). However, the presence of fast travelling gravity and Lamb waves limits the maximum size of the time-step that may be used in the adjustment step. It may be noted that the absence of Lamb waves in the NHAD model significantly alleviates the restrictions on the maximum size of time-step allowed in this model.

- The C-grid (e.g. Mesinger and Arakawa, 1976; Arakawa and Lamb, 1977) is used in the MP and NHAD models (Xue and Thorpe, 1991; Room et

al., 2001). The split semi-Lagrangian scheme is formulated on a grid that is nonstaggered in both the horizontal and vertical (the Arakawa A grid).

- The quasi-elastic σ coordinate equations are formulated independent of a thermodynamic reference profile (see Chapter 3), and the split semi-Lagrangian procedure is also formulated free of the use of a reference profile. In the MP and NHAD models, the temperature and geopotential fields are formulated as deviations of a thermodynamic reference profile. Since the reference profile depends on pressure that may be changing as a function of time on the σ levels, the reference profile needs to be updated at regular time intervals (see Xue and Thorpe, 1991). Additonally, the use of a reference geopotential profile complicates the solution of the elliptic equation for the geopotential deviation in the MP-models (Xue and Thorpe, 1991).

- In the numerical realizations of the σ coordinate MP-model, the vertical momentum equation is used explicitly for the calculation of the vertical motion field. In nonhydrostatic meso-scale circulation systems, the horizontal and vertical velocities are often of the same scale of magnitude. Under these circumstances, it may be advantageous to discretize the horizontal and vertical momentum equations in a similar fashion, by calculating both the horizontal and vertical motion fields directly from these equations. However, during the early development stage of the new numerical model developed in this study, it was attempted to use the vertical momentum equation explicitly to calculate the vertical motion field by means of an advection and adjustment step (silmilar to the approach presently used to calculate the horizontal wind). It was found that the calculation of the vertical motion field in this fashion, and the calculation of the surface pressure by means of the continuity equation, leads to an important inconsistency in the split semi-Lagrange procedure. Therefore, in the present version of the split semi-Lagrangian scheme, the vertical motion and surface pressure are calculated consistently from the continuity equation. The vertical momentum equation is not used explicitly, but is incorporated in the elliptic equation used to diagnose the geopotential. In the NHAD-model, the vertical motion field is also diagnosed from the continuity equation. However, in the latter model there is no prognostic eqution for the surface pressure (Room et al., 2001; also see Chapter 2). The approach in the split semi-Lagrangian scheme to obtain $\dot{\sigma}$ and p_s consistently from the continuity equation bears close resemblance to the solution procedure followed in hydrostatic σ coordinate models. This facilitates the development of a hydrostatic global or regional model to a nonhydrostatic model based on the quasi-elastic equations.

- In the σ coordinate MP and NHAD models, the elliptic equation for the geopotential is solved by an intricate procedure involving a Fast Fourier Transform method (Xue, 1989; Xue and Thorpe, 1991; Room et al., 1991; also see section 4.6). Some general software is required for this purpose

(Xue, 1989). During the development phase of the new model in the present study, it was thought best to have an independently coded elliptic solver available. A SOR procedure was therefore developed to solve the elliptic eqution in the geopotential, in two or three spatial dimensions (see section 4.6). This procedure is reasonably efficient (see Chapter 5), but it may be advantageous to implement a FFT method in the model for more efficient solution of the elliptic equation in the future.

4.11 Discussion

Chapter 4 reports on the development of a novel split semi-Lagrangian scheme formulated to solve the quasi-elastic σ coordinate equations on a nonstaggered grid. The main features of the new dynamic kernel are:

- nonhydrostatic, quasi-elastic formulation using a terrain-following coordinate based on the full pressure field;
- two time-level, time-split time integration scheme involving an advection, adjustment, spatial filtering and spatial smoothing step;
- spatial discretization on a horizontally and vertically nonstaggered grid;
- semi-Lagrangian advection for the horizontal wind, surface pressure and temperature, using McGregor's method for the calculation of departure points and bicubic spatial interpolation;
- high-order accurate centered differencing on the nonstaggered grid;
- high-order, highly scale-dependent Shapiro spatial filtering;
- option of explicit diffusion available;
- consistent evaluation of the surface pressure and vertical motion field by using the continuity equation;
- semi-implicit treatment of the Coriolis terms;
- three-dimensional iterative solution of a variable-coefficient, non-linear elliptic equation for the geopotential at each adjustment time-step, using SOR.

A distinguishing feature of the split semi-Lagrangian scheme, is its formulation on a nonstaggered grid. This set-up is very attracive from a computational point of view, since only one set of departure points needs to be calculated at each advection step of the model. However, it is well-known that the nonstaggered grid has poor gravity wave dispersion properties (see sections 4.3 and 4.8). These may be improved by the use of high-order spatial differencing on the nonstaggered grid (sections 4.3 and 4.8). However, the presence of stationary two-grid-interval waves remain problematic. These waves are filtered with

a high-order spatial Shapiro filter (see sections 4.4 and 4.5.3). This filter has a negligible damping effect at longer wave lengths, but completely removes the two-grid-interval waves. The explicit diffusion step (section 4.5.4) is not required for numerical stability considerations, but may be needed in order to obtain a grid-converged solution (see section 4.5.4 and Chapter 5).

A traditional stability analysis (see Mesinger and Arakawa, 1976) of the adjustment step of the split semi-Lagrangian scheme has not been presented in this Chapter. There appears to be no straight forward way to find an analytic result in this regard, because of the complicated nature of the σ coordinate quasi-elastic equations. However, for the case of linear advection, the semi-Lagrangian procedure used in the advection step is known to be unconditionally stable (see section 4.2). The frequency response of the adjustment step equations to the forward-backward scheme (see section 4.7) also provides some indication of how the gravity waves function to limit the maximum size of time step that may be used in the adjustment step. In Chapter 5 the stability properties of the full scheme are examined by means of numerical experiments. It is shown that the split semi-Lagrangian scheme is stable at large Courant numbers during the advection step. Fast travelling gravity and Lamb waves limit the size of the time-step that can be used in the adjustment procedure. The large time-steps allowed during the advection step, represent the main computational advantage of the split semi-Lagrangian scheme over the explicit procedures used in the MP and NHAD models. In fact, the split semi-Lagrangian approach may even in some cases offer computational advantages over the widely used, highly efficient, semi-implicit time differencing schemes.

In recent years, semi-implicit time integration schemes (e.g. Robert, 1969; Tapp and White, 1976) have become very popular for use in NWP and climate simulation models (e.g. Cullen, 1990; Tanguay et al., 1990; McGregor and Dix, 2001; Davies et al., 2005). This popularity is to a large extent linked to the development of models based on the fully-elastic, non-hydrostatic equations. These models contain acoustic waves as part of their solution set (see Chapter 1). The semi-implicit schemes neutralize the computational disadvantage caused by the presence of acoustic waves in the fully-elastic equations, without compromising the treatment of motion at spatial scales relevant to current NWP and climate simulation (Tapp and White, 1976; Tanguay et al., 1990, Davies et al., 2005). However, the stability of semi-implicit schemes at long time steps is achieved by spuriously retarding the fast-propagating acoustic and gravity waves responsible for the time step limitations of explicit schemes (e.g. Davies et al., 2003). For high-resolution, meso-scale applications of a nonhydrostatic model, the fast propagating gravity waves may be important in their own right, and the time-step used in a given semi-implicit scheme may have to be shortened in order to represent the dynamics and physics of the motion properly (e.g. Davies et al., 2003). Thus, the time-step advantage offered by semi-implicit schemes over explicit schemes would be lost. It is for cases such as

these where split semi-Lagrangian formulations may provide the most appealing choice of time integration scheme, from the perspective of computational efficiency. Even for situations where the fast moving gravity waves carry a non-negligible amount of the energy, the split semi-Lagrangian approach allows the use of relatively large time steps for the simulation of the much slower advection process. The fast moving gravity and sound waves may be accurately treated during the adjustment procedure involving a much smaller time-step. However, the explicit schemes and semi-implict schemes would be limited to the use of small time-steps, because of stability and accuracy considerations respectively.

At larger spatial scales, where the fast moving gravity waves are not important in their own right and may be parameterized (for orographic gravity waves, in the case of numerical weather prediction and climate simulation), semi-implicit time integration offers computational advantages over the split semi-Lagrangian approach. In the latter case, the adjustment step would be limited to relatively small values because of the presence of the fast moving gravity and sound waves. However, the semi-implicit schemes will be stable at much larger time steps because of the spurious retardation of the fast-moving waves by these schemes. Thus, the potential computational advantages of the split semi-Lagrangian approach are limited to high-resolution micro and meso-scale studies where the accurate representation of fast-moving gravity waves is important.

The split semi-Lagrangian scheme may also offer a computational advantage over traditional split-explicit procedures where Eulerian discretization is used for the advection terms. Janjic (2001) stated that the advection step in (Eulerian) time-split solutions of the atmospheric equations used in numerical weather prediction is limited by the CFL condition to values of about three times the adjustment time-step. This is beacuse the wind speed can exceed $100\,ms^{-1}$, compared to the speeds of up to $300\,ms^{-1}$and $350\,ms^{-1}$for gravity and sound waves respectively. However, the statement of Janjic does not hold when a split semi-Lagrangian method is used to solve the advection terms in the governing equations. The linear analysis in section 4.2 (following McDonald, 1984) indicates that the semi-Lagrangian scheme applied in the present study is unconditionally stable for the case of linear advection. The numerical results shown in Chapter 5 for highly non-linear flow illustrate that when the time-split method employs a semi-Lagrangian approach to solve the advection terms, advection time-steps at Courant numbers larger than unity may be used, without comprimising the numerical stability of the scheme. This yields a computational advantage over Eulerian split-explict schemes.